

NY 2-2

USSIO / LIBRARY

NASA CR

STUDY OF COLOR CENTER FORMATION IN WHITE POWDER COMPOUNDS

By

Herman Levin
Cedric C. Berggren
Willard M. Peffley

DECEMBER 1970

Distribution of this report is provided in the interest of information exchange.
Responsibility for the contents resides in the author or organization that prepared it.

FACILITY FORM 602	N71-28044	
	(ACCESSION NUMBER)	(THRU)
	83	G3
	(PAGES)	(CODE)
	CR-118865	24
	(NASA CR OR TMX OR AD NUMBER)	(CATEGORY)

Prepared under Contract No. NAS 2-5034 by
HUGHES AIRCRAFT COMPANY
Culver City, California

for

AMES RESEARCH CENTER
NATIONAL AERONAUTICAL AND SPACE ADMINISTRATION



NASA CR-

STUDY OF COLOR CENTER FORMATION IN WHITE
POWER COMPOUNDS

by

Herman Levin
Cedric C. Berggren
Willard M. Peffley

Distribution of this report is provided in the interest of
information exchange. Responsibility for the contents
resides in the author or organization that prepared it.

Prepared under Contract No. NAS 2-5034 by
HUGHES AIRCRAFT COMPANY
Culver City, California

for

AMES RESEARCH CENTER
NATIONAL AERONAUTICAL AND SPACE ADMINISTRATION

FOREWORD

This report was prepared by the Hughes Aircraft Company, Research and Development Division, Aerospace Group for the National Aeronautics and Space Administration. The work was administered by the Ames Research Center. Mr. Don L. Anderson was project monitor.

This summary report covers work accomplished during the period September 1, 19~~69~~⁷⁰ through September 30, 1970.

Mr. Herman Levin, Mr. Cedric C. Berggren, and Mr. Willard M. Peffley were principal investigators. Mr. Paul M. Blair, Jr. was project engineer. The work was conducted within the Materials Technology Department under the direction of Mr. L. Brian Keller. Dr. Ferdinand A. Kröger, Chairman of the Materials Science Department, University of Southern California, contributed as a consultant.

The authors gratefully acknowledge the major contributions to the earlier part of the effort by their former associate Dr. V. M. Honnold. They also wish to express their sincere appreciation to the following:

Dr. A. L. Gentile and Dr. O. M. Stafsudd - for many helpful discussions and the use of their preparatory facilities

Dr. J. L. Kolopus and Mr. C. T. Butler of the Oak Ridge National Laboratory - for many helpful discussions and certain starting materials

Mr. Charles J. Bahun - for his kindness in performing certain mathematical analysis

Mr. Mike N. Gardos - for his able assistance during the experimental work

Mr. David E. Schnelker and Mr. Jerg B. Jergenson - for their outstanding effort in getting the irradiation gear on-stream

Mr. Charles H. Fetters - for his capable fabrication of quartz-ware

ABSTRACT

An experimental investigation of typical foreign (impurity) defects and native defect generation by low energy protons has been performed. In-situ (vacuum) optical and spin resonance spectra were obtained which upon resolution revealed individual defect species and their densities. Analysis of these data provided a basis for correlating the growth kinetics of various color centers, including those associated with substitutional impurities and those associated with native lattice defects. In contrast to earlier theoretical work wherein discoloration was thought restricted to the proton range, it is now established that the dominant coloration mechanism consists of electron-hole pair diffusion into the crystal bulk (from a surface layer in which they are generated - proton range) followed by recombination and trapping in the bulk. This diffusion-dependence in the bulk (rather than proton displacement in the surface layer) greatly increases the influence of initial defect structure on the resultant optical damage.

PRECEDING PAGE BLANK NOT FILMED

CONTENTS

1.0	INTRODUCTION	1
2.0	EXPERIMENTAL	3
2.1	Proton Irradiation Facility	3
2.2	Optical Measurements	5
2.3	Electron Paramagnetic Resonance (EPR).	7
2.4	Materials: Effects and Preparation	
2.4.1	Hydrogen.	14
2.4.2	Elements of First Transition Series.	15
2.4.3	Alkali Metal Cations	18
2.4.4	Miscellaneous Cations	18
2.4.5	Anion Impurities.	18
2.4.6	Fe ³⁺ -Doping Procedure	19
3.0	COLOR CENTER GENERATION IN MgO	23
3.1	Powder Experiments	23
3.2	Single Crystal Experiments	25
3.2.1	Effect of Controlled Chemical Processing.	25
3.2.2	Effect of Selected Impurities.	30
3.3	Point Defect Identification by Spin Resonance	34
4.0	COLOR CENTER GENERATION KINETICS IN MgO	41
4.1	Evidence for Charge Carrier Diffusion.	42
4.2	Optical Damage Kinetics	43
4.2.1	Band Gap Considerations	43
4.2.2	Growth Rate of Fe ³⁺ Band in the Bulk	45
4.2.3	Growth Rate of V ₁ Center	49
4.2.4	Kinetics of Miscellaneous Centers	55
4.2.5	Effect of Dose Rate on Generation Kinetics	55
5.0	SUMMARY	59
6.0	REFERENCES	61
	APPENDIX A	A-1
	APPENDIX B	B-1

ILLUSTRATIONS

<u>Figure</u>		<u>Page</u>
1	Proton irradiation and optical measurement facility	3
2	Schematic of modifications in Cary 14 optical system	6
3	EPR spectrometer system	8
4	Block diagram of EPR electronics	9
5	Loaded microwave cavity arrangement in EPR spectrometer	10
6	Chen and Sibley ² data for γ -radiation induced maximum V_1 center absorption as a function OH ⁻ content in MgO single crystals from various sources	16
7	Absorption change in MgO powder (compressed) induced by a 1.0 keV neutralized proton beam at 20°C and 10^{-5} torr H ₂ (F1799-43)	24
8	Change in optical absorption induced in processed, high purity MgO single crystal by neutralized 1.0 keV proton beam at 20°C and 10^{-5} torr H ₂ (F1799-63) . .	27
9	Change in spectral absorption coefficient induced in high purity MgO single crystal by neutralized 1.0 keV proton beam at 20°C and 10^{-5} torr H ₂ (F1799-63) . .	28
10	Change in spectral absorption coefficient induced in high purity MgO single crystal by neutralized 1.0 keV proton beam at 20°C and 10^{-5} torr H ₂ (F1799-55) . .	29
11	Change in optical absorption induced in low purity MgO single crystal by a neutralized 1.0 keV proton beam at 20°C and 10^{-5} torr H ₂ (F1799-66) . .	31
12	Change in spectral absorption coefficient induced in low purity MgO single crystal by a neutralized 1.0 keV proton beam at 20°C and 10^{-5} torr H ₂ (F1799-66) . .	33
13	Effect of gamma-irradiation (in vacuum at 20°C) on EPR spectra (79°K) of air-quenched, moderate purity, single crystal MgO	37
14	Estimated electron energy level diagram for selected defects in MgO	44
15	Measured growth of Fe ³⁺ density induced in the bulk of various MgO single crystals by 1.0 keV proton irradiation (neutral beam) at a flux of 3.0×10^{11} to 3.4×10^{11} p ⁺ /cm ² -sec	46

ILLUSTRATIONS (Continued)

<u>Figure</u>		<u>Page</u>
16	Estimated p^+ -induced growth to saturation of Fe^{3+} in the bulk of two MgO single crystals	50
17	Measured growth of V_1 center induced in various MgO single crystals by 1.0 keV proton irradiation (neutral beam) at a flux of 3.0×10^{11} to 3.4×10^{11} p^+/cm^2 -sec	54
18	Measured growth of 3.6 eV band in various MgO single crystals by 1.0 keV proton irradiation (neutral beam) at a flux of 3.0×10^{11} to 3.4×10^{11} p^+/cm^2 -sec	56
A1	Optical reflectance schematic	A2

TABLES

<u>Table</u>		<u>Page</u>
1	Concentration of Selected Impurities in Various MgO Specimens (Parts Per Million Atomic)	13
2	Processing Effects on $\text{Fe}^{3+}/\text{Fe}^{2+}$ Distribution in Single Crystal MgO	16
3	Fe^{3+} -Doping of High Purity Single Crystal MgO	20
4	Selected Defect Determinations Obtained From Corresponding EPR and Optical Data	35
5	Estimated Fe^{3+} Growth Rate Dependence in the Bulk	49
6	Comparison Between Computed and Experimental Normalized Growth Rates for Fe^{3+} in the Bulk	51
7	Scaling Factors for Comparing the Growth Rate of V_1 Center ($dV_1/dt = d_{pH}/dt$) in Experiments (-66) and (-71)	55

1.0 INTRODUCTION

The work reported herein represents an experimental investigation of the discoloration of MgO by low energy proton irradiation. It constitutes a continuation of the first year's theoretical study. Experimentation was restricted to MgO, both single crystals and polycrystalline material, as typical of a dielectric with application to thermal control coatings.

Certain material preparation efforts were carried out. These included carefully controlled high temperature processing and selective doping of single crystal specimens with iron.

Discoloration effects were introduced by bombarding specimen targets with 1.0 keV protons (neutral beam) delivered at controlled rates in vacuum at room temperature. In-situ (vacuum) measurement of optical and EPR spectra were obtained and analyzed to demonstrate proton-induced defect species and generation rates. These kinetic data were then correlated in terms of individual color centers important to solar energy absorption. The relevance of accelerated laboratory simulation to real time in space was also indicated.

Practical demonstration of the control of certain material parameters to obtain radiative stability is also presented.

2.0 EXPERIMENTAL

The experimental portion of this effort was restricted to an investigation of damage induced in magnesium oxide (MgO) by low energy protons (1.0 keV) incident at an order of 1000 x the solar wind proton flux. The effort involved measurement of changes in optical and EPR spectra resulting from controlled proton dose.

2.1 PROTON IRRADIATION FACILITY

This facility is shown in Figure 1. Appearing in the lower center is an eight inch O.D., horizontal, vacuum station connected to a 400 l/s ion pump (Hughes Aircraft Company, Vacuum Tube Products Division) at bottom center. A single Vac-Sorb, roughing pump is also shown attached to the station.

Attached to the top of the station through a 1-1/2 O.D. entry is the proton source (seen in the center of the photograph). This is a

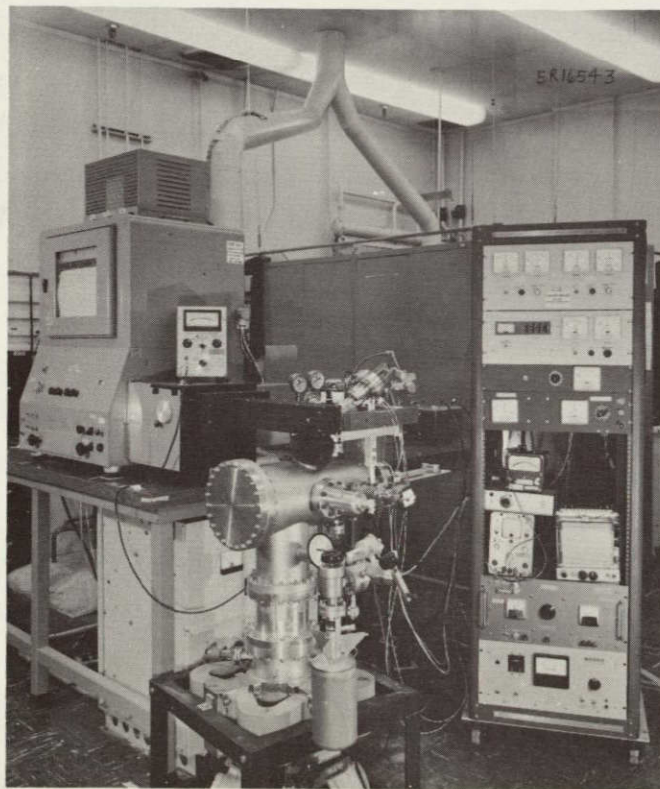


Figure 1. Proton irradiation and optical measurement facility

NOT REPRODUCIBLE

trapped electron ionization source and was constructed by H. J. King and D. E. Schnelker of Hughes Research Laboratories. It is described in detail by King and Zuccaro¹ in their definitive study, "Solar Wind Simulation Techniques." It provides a H^+ beam (>99 percent purity) of uniform intensity over a diameter of 2.5 cm at the target specimen. Flux is variable over several orders of magnitude, and proton energy is variable up to 3.0 keV. The associated gun electronics are shown at the right enclosed in a free standing console. These were designed and developed by J. Simpkins of Hughes Research Laboratories. They include a single feedback loop to provide flux control.

At the upper left in Figure 1 is a Cary Model 14 spectrophotometer. Modifications of terminal optics in the instrument (enclosed in black painted housings) permit its scanning beams to be folded into an integrating sphere mounted within the vacuum station.

Specimen movement within the station, e. g. between irradiation and optical measuring positions, is accomplished by means of a push-pull, rotary mechanism. Despite its use of a lubricated (Apiezon Number L) O-ring seal, this mechanism gave no evidence of introducing impurities which could serve to confuse the experimental work.

Accessories included a Faraday cup ($1. \text{cm}^2$ opening) movable to the sample position by a bellows-sealed transfer arm. A nitrogen gas aspirator was used to rough-pump the station, followed in turn by a sorption pump. Sample recovery in vacuum (at the end of an experiment) was accomplished by a 10 mm O. D. Suprasil II (fused quartz) tube attached to the station just beneath the sample position by means of a graded glass seal-Kovar-soft copper-2-3/4" O. D., S. S. flanged compression port connection. Sample removal was effected by "pinch-off" at the copper tabulation. Manual control of the hydrogen gas flow to the ionizing gun was accomplished with a variable leak valve (Granville-Phillips Company Number 203019-02).

2.2 OPTICAL MEASUREMENTS

A Cary recording spectrophotometer (Model 14) was used to obtain in-situ reflectance measurements before, during and upon termination of the particulate radiation. These measurements required about 30 minutes and were made on the specimen by quickly moving it from the irradiation position into the center of an integrating sphere located within the vacuum station. Accounting for the time required for instrument referencing, the specimen remained out of the p^+ beam for a total of about 15 minutes of the 30 minute measurement period. Because of noise associated with the e^- -source, it was found necessary to shut off the neutralizing e^- -beam during the entire 30 minute period.

Certain terminal optics of this dual beam spectrophotometer were modified (see Figure 2) in order to permit its use for making reflectance measurements in-situ. First, the IR detector compartment was replaced with an IR lamp (6 v., 18 a.), thus reversing the IR beam path. Second, the UV/visible detector compartment was removed in order to permit both the reference and sample beam paths (all modes: near UV, visible, and IR) to be folded into the integrating sphere (smoked MgO). This was accomplished as indicated by a pair of 2 inch O.D. x 3.84 F.L. spherical mirrors, a pair of 2 inch x 2 inch x 1/4 inch plane mirrors, and a single 2 inch O.D. x 5.91 F.L. spherical mirror. These mirrors were all first surface aluminum vapor deposited on optical grade pyrex (annealed), overcoated to provide >85 percent reflectance between 0.2 and 2.5μ , and mounted in a light tight duct. The total increase in optical path was an order of 30 inches. This increase, coupled with the necessity of beam stopping imposed by the dual requirements of reference/sample beam segregation and minimization of the sphere entry port, resulted in some signal attenuation. As a result, the lower limit of UV operation increased from a nominal 200 nm (without dry N_2 purging) to 235 nm. Operation in the visible region was unaffected. The upper limit of IR operation dropped to 1600 nm from a typical 2600 nm (2.6μ) despite limited efforts involving the use of other IR sources of increased emission and

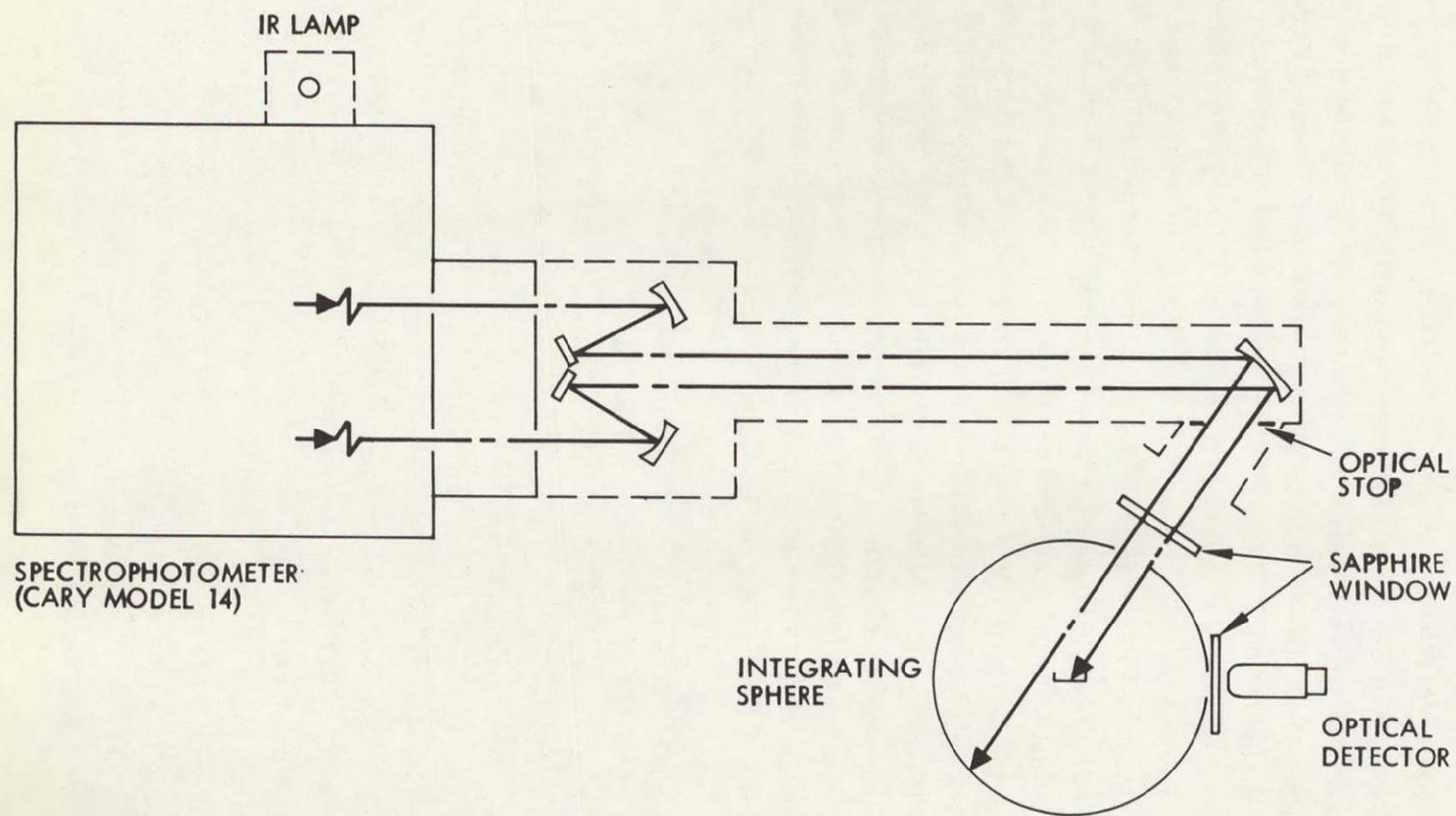


Figure 2. Schematic of modifications in Cary 14 optical system

varying geometry. Since optically detectable defect structure in MgO in the 0.8-2.5 μ region is quite small, the spectral limitation in IR range did not prove a handicap.

Interchangeable detectors were inserted into the detector port of the vacuum station. The pre-focused PbS cell used by the Cary for IR detection was retained. An EMI Number 9601B photomultiplier tube (S-11 response) was used for near-UV/visible detection, replacing the 1P28 (S-5 response) photomultiplier previously used. This change was designed to improve sensitivity in the visible region without serious loss in the near-UV region.

Experimental single crystal specimens were arranged in an aluminum mount (0.750 I.D.) in a close fitting mosaic pattern of 5-0.5 cm x 0.5 cm x 0.09 cm (approximately) crystal wafers, resting on a second surface, aluminized Suprasil mirror substrate. Upon termination, these crystals were quickly dropped into an EPR specimen tube designed to sandwich all five together in a common $\langle 100 \rangle$ alignment.

2.3 ELECTRON PARAMAGNETIC RESONANCE (EPR) MEASUREMENTS

In the context of an experimental matrix of (a) selective impurity doping (b) controlled pre-irradiation processing and (c) control of absorbed radiation, EPR measurements can provide valuable data to supplement that obtained from optical reflectance spectroscopy. Such data prove helpful to mechanism studies in the following ways:

- a. Detection of paramagnetic centers
- b. Assist in identification of paramagnetic center
- c. Determine concentration of paramagnetic species and thus permit study in terms of generation or annealing kinetics
- d. Help to define the nature of the species surrounding the paramagnetic center.

Low temperature (e.g. 77°K) EPR measurements performed on irradiated specimens "in situ" represent the preferred measurement technique. Unfortunately the short range of 1 kev protons (the particulate radiation source) requires a relatively large specimen surface area for exposure to radiation in order to induce a detectable number of spins (e.g., 10^{14} to 10^{15} spins). In turn, this imposes a need for a large-access microwave cavity and a special quartz dewar, both of which were acquired for this program.

A modified Varian EPR spectrometer (model V-4500, reflection homodyne type) employing 100 kHz modulation of the magnetic field supplied by a 12 inch magnet (Varian V4012, variable yoke) was used. This system, including associated electronic gear, is shown in Figure 3. A block diagram of the spectrometer electronics used is given by Figure 4. Indicated is a swept frequency oscillator (SFO) used to determine the resonant microwave frequency for a given cavity loading at a given temperature (i.e., specimen, specimen tube, dewar,

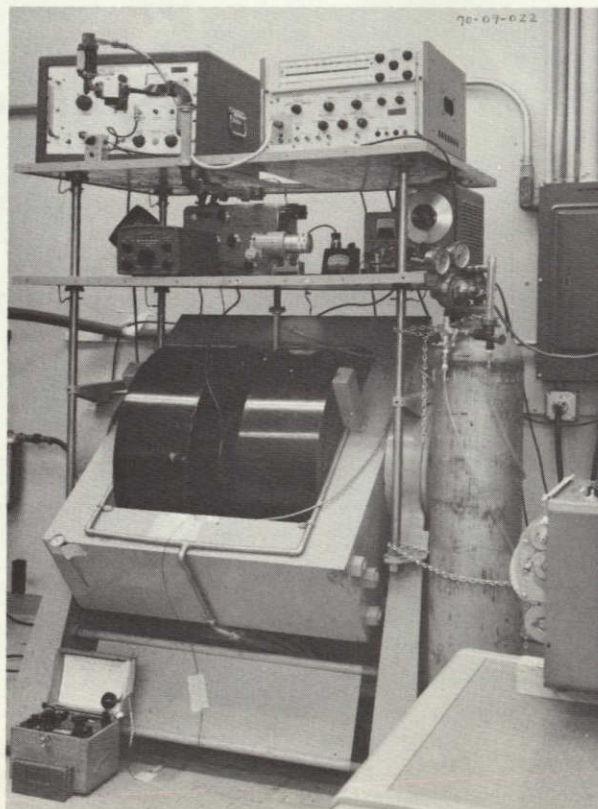


Figure 3. EPR spectrometer system

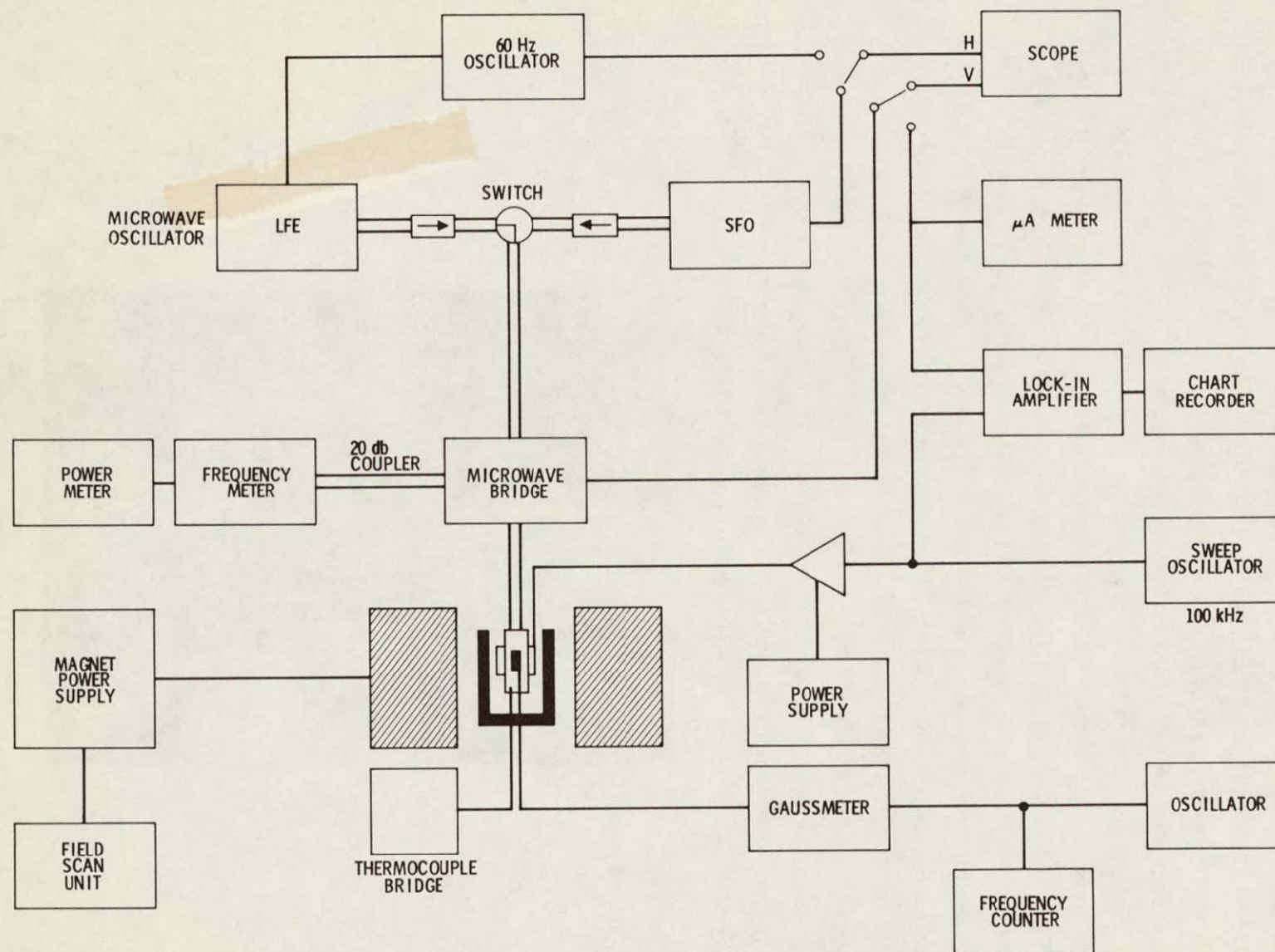
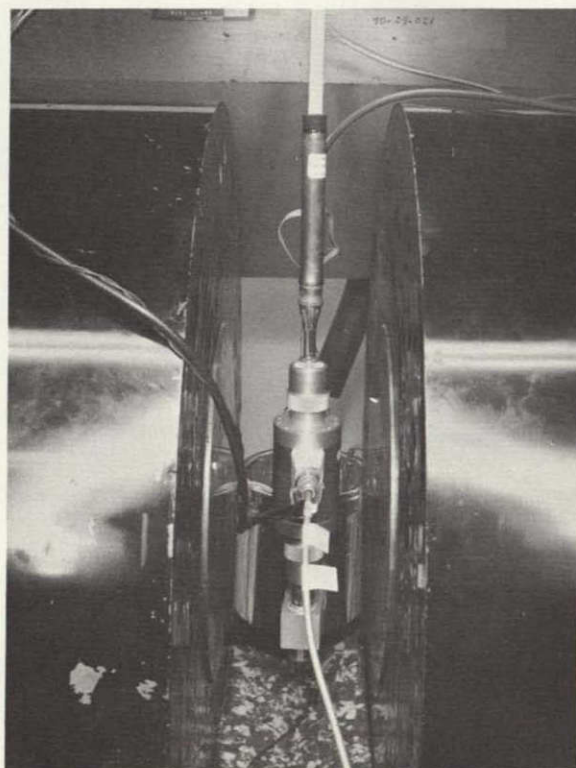


Figure 4. Block diagram of EPR electronics

cold gas, etc.). Microwave power at this frequency is then introduced into the Varian microwave bridge, using as a source an ultra-stable microwave oscillator (Laboratory for Electronics Number 814-A-X-21, 8.5 to 10.0kHz) instead of the Varian klystron oscillator. The spectrometer is operated in the X-band near 9200 MHz. Note that it was found necessary to alter the resonant frequency of the cavity (by the insertion of two aluminum rings) in order to locate the desirable TE_{013} mode near the mid-range of the LFE oscillator. A lock-in amplifier (Princeton Applied Research Number HR-8) is employed for modulation and phase detection of the EPR signal which is displayed on a strip recorder. A nuclear magnetic resonance precision gaussmeter (Harvey-Wells Number G-501) was used to measure the magnetic field intensity associated with the display of a given EPR signal. The proton probe of the gaussmeter is seen mounted (Figure 5) adjacent to the microwave cavity in the homogeneous field of the 12-inch magnet. This magnetic field value, coupled with the value of the



NOT REPRODUCIBLE

Figure 5. Loaded microwave cavity arrangement in EPR spectrometer

microwave frequency, permits the determination of the g-values (see Appendix B) of the resonance lines in the EPR spectrum.

Supported in the center of the magnetic field is a large sample access cavity (Varian V-4535, 2.5 cm diameter access) in which was inserted a quartz dewar (Varian P/N 909005-01, 11. mm I.D.). Cold nitrogen gas ($\sim 80^\circ\text{K}$), from a liquid N_2 chiller-transfer system, was passed up through the dewar and around the evacuated specimen tube contained therein. This arrangement of specimen tube-dewar-microwave cavity - cold gas system is shown between magnet pole pieces in Figure 5. The Q of this cavity-dewar-sample tube configuration has been measured to be about 6600 and provides an optimum sensitivity of approximately 5×10^{14} spins.

2.4 MATERIALS: EFFECTS AND PREPARATION

As a preface to this section it is important to point out the dominant role played by lattice-soluble impurities in determining the optical changes introduced by radiation. Further, as will be demonstrated in Section 3.0, the magnitudes of these effects may be significantly influenced by the thermal treatment imposed during or subsequent to initial preparation. It is equally important to recognize that, although MgO has received more research attention than any other alkaline earth- or refractory-oxide in terms of radiation-induced optical changes, precise definition of the effect of individual impurities (either substitutional or interstitial) in varying matrices of other foreign (extrinsic) and native (intrinsic) defects remains a distant goal. Typical of the problem, as recent as 1967 Chen and Sibley² reported that V_1 center generation in MgO by ionizing radiation (important here) was crystal-dependent. The nature of this dependency could not be identified. They did find that very fast quenching (e.g., $23^\circ\text{C}/\text{sec}$) from temperatures between 500 and 1250°C prior to irradiation could increase resultant V_1 densities by as much as five-fold, depending on the source of the crystal. They also reported that Co, Cr, Mn, and Ti act to suppress V_1 center production. Dr. J. L. Kolopus³, an

associate in the above work, states this particular problem has not yet been resolved and probably will require an ultra-pure (e.g., 1-2 ppma total impurities) target material for its resolution. Parallel work reported by Glass and Searle¹¹, while not conclusive, did indicate that an increase in isolated magnesium ion vacancies results from such thermal treatment, yielding an increased density of V_1 centers. They pointed out that "cation vacancies and impurities are essentially immobile in MgO below about 400°C."

Despite the above mentioned data limitations, it is believed that the present state-of-the-art in MgO is sufficiently advanced to permit significant progress toward obtaining a truly radiation-stable pigment. The relatively simple, cubic symmetry of MgO provides another reason for selecting this compound, from among other white dielectric oxides, for initial experimentation. The work of the program was thus confined to MgO, powder and single crystal.

Reagent grade powder (Mallinckrodt Chemical) of relatively low purity was hydraulically compressed (50-70 kpsi) at room temperature. Easy delamination of the pressed discs permitted random chip selection from within the pressed body. A weighed amount of these irregular chips (~0.4 cm x 0.4 cm x 0.13 cm) constituted the proton target. They were not annealed or given other thermal treatment prior to irradiation. The intent was to use the impure powder spectra (both optical and EPR) for initial study as a guide to the overall defect structure. Despite the availability of high purity powder, subsequent experimentation was carried out with single crystal MgO in order to obtain "cleaner" spectra. This is especially true of EPR spectra because of orientation dependency associated with anisotropic defects.

Single crystal MgO was obtained from two sources. High and moderate purity material was provided through the courtesy of C. T. Butler from the Research Materials Program of the Solid State Division of the Oak Ridge National Laboratory. Low purity material was obtained from the Norton Company (optical quality "Magnorite"). In terms of possible substitutional replacement of lattice ions, the impurities selected in Table 1 are likely candidates. In this manner they can

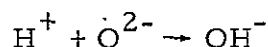
Table 1. Concentration of Selected Impurities in Various MgO Specimens
(Parts Per Million Atomic)

Element	Detection Limit, ppma	Compressed Powder-Very Low Purity (-43) ppma $10^{17}/\text{cm}^3$	Single Crystal, ppma				
			Low Purity-N ₂ Processed (-66)	Moderate Purity: Air-Quenched (-71)	High Purity-As Received (-55)	High Purity-N ₂ Processed (-63)	High Purity: Fe-doped, Air-Quenched (-67)
Li	1.	**	4.9	5.1	6	6.	6.
B	19.	nd	nd	nd	nd	nd	18.6
N	--	**	**	2.9 *	7.2 *	7.2 *	7.2 *
F	--	**	**	<1. *	<1. *	<1. *	<1. *
Na	0.1	830.	28.7	2.2	9.3	12.2	nd
Al	3.7	12.7	16.4	11.2	11.9	nd	10.4
Si	14.	108.	20.8	--	23.6	38.7	36.5
P	--	**	**	2.6 *	26. *	26. *	26. *
Ti	4.2	nd	1.3 *	1.3 *	nd	nd	nd
V	4.0	nd	nd	nd	nd	nd	nd
Cr	0.4	nd	1.3	nd	nd	nd	nd
Mn	1.5	nd	20.6	nd	nd	21.6	nd
Fe	1.8	7.6	39.7	8.0	2.0	5.4	541.
Co	1.7	nd	nd	nd	nd	nd	nd
Ni	1.4	nd	1.6	nd	nd	nd	nd
Cu	0.2	1.2	0.3	0.4	0.3	0.4	0.4
nd - not detected (below detection limit) *Estimate **Not determined							

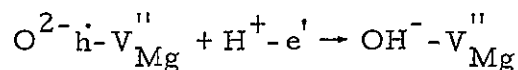
generate intrinsic defect structure initially and during irradiation quench-in radiation-induced defect structure as trapping sites, individually or in association with intrinsic defects. With the exception of Li and Na (determined by flame photometry and atomic absorption analysis respectively) and N and F (estimated from typical analyses on this material previously made), the remaining elements were obtained from arc emission analyses. It was originally intended to use spark source mass spectrometry in order to obtain <1 ppm detection limits, but as the work proceeded such improved sensitivity did not seem required, with the possible exception of boron.

2.4.1 Hydrogen

Hydrogen analyses were not obtained. This may represent an important omission from Table 1. The degree of importance probably relates to the density of OH^- , either resulting from (a) original preparation procedures or from (b) proton irradiation. The latter case might include both proton (H^+) stopping in the "surface":



and diffusion of charge equilibrated hydrogen atom ($\text{H}^+ - e'$) interstitials into the bulk with capture at a V_1 center, i. e., the latter described as a hole h localized on an O^{2-} adjacent to a magnesium ion vacancy, V_{Mg}'' :



Henderson and Wertz⁴ review this area in detail because "it has led to a description of the geometry of one stable site for hydrogen in an oxide." Current infrared studies indicate that substitutional OH^- in isolated sites is displayed optically by a broad band centered at a wave number of 3400 cm^{-1} ($\lambda \approx 2.94 \mu$), with the hydrogen atom suspected of

being directed interstitially¹¹. Additionally, in unirradiated crystals containing OH⁻ a strong, narrow band is displayed at 3296 cm⁻¹ ($\lambda \approx 3.03\mu$). This has been associated with the axially aligned "trio", O²⁻H⁺-V["]_{Mg} (equivalent to OH⁻-V["]_{Mg}). Upon ionizing irradiation, the 3296 cm⁻¹ band is shifted to 3323 cm⁻¹ (3.0 μ) with attendant generation of a strong EPR signal. This latter is associated with the axially aligned "quartet", OH⁻-V["]_{Mg}-O⁻, where O⁻ represents a h[•] localized on a normal lattice oxygen ion. Note that all three above spectra are more prominent in MgO single crystal prepared from Mg(OH)₂ powder than from MgCO₃ powder. The anisotropic defect, OH⁻-V["]_{Mg}-O⁻, has been termed the V_{OH} center.

Interestingly enough, examination of Chen and Sibley's² data (Figure 6) reveals that ionization-induced V₁ center saturation is inversely proportional to OH⁻ density prior to irradiation. Their data, which include crystals from various sources with random variations in total iron of 5-100 ppm and total chromium of 1-20 ppm etc., are presented in Figure 6. If the ultimate fate of a significant portion of low energy protons stopped in a target is to form OH⁻, this may also explain part of the difficulty during this work of generating larger densities of V₁ centers by proton irradiation.

The role of OH⁻, both isolated and associated with V["]_{Mg}, in radiative coloration of MgO warrants further attention. Such investigation was not pursued during this work because other aspects appeared more pressing.

2.4.2 Elements of First Transition Series

Ions of this series have received the most attention and have been shown to significantly affect radiation coloration processes. The more important of these are as follows:

<u>Ion</u>	<u>Preferred Valence State</u> ⁵
Fe ¹⁺ , Fe ²⁺ , Fe ³⁺	Fe ²⁺
Cr ²⁺ , Cr ³⁺	Cr ³⁺
Ti ³⁺ , Ti ⁴⁺	Ti ⁴⁺
Mn ²⁺	Mn ²⁺
Co ¹⁺ , Co ²⁺	Co ²⁺

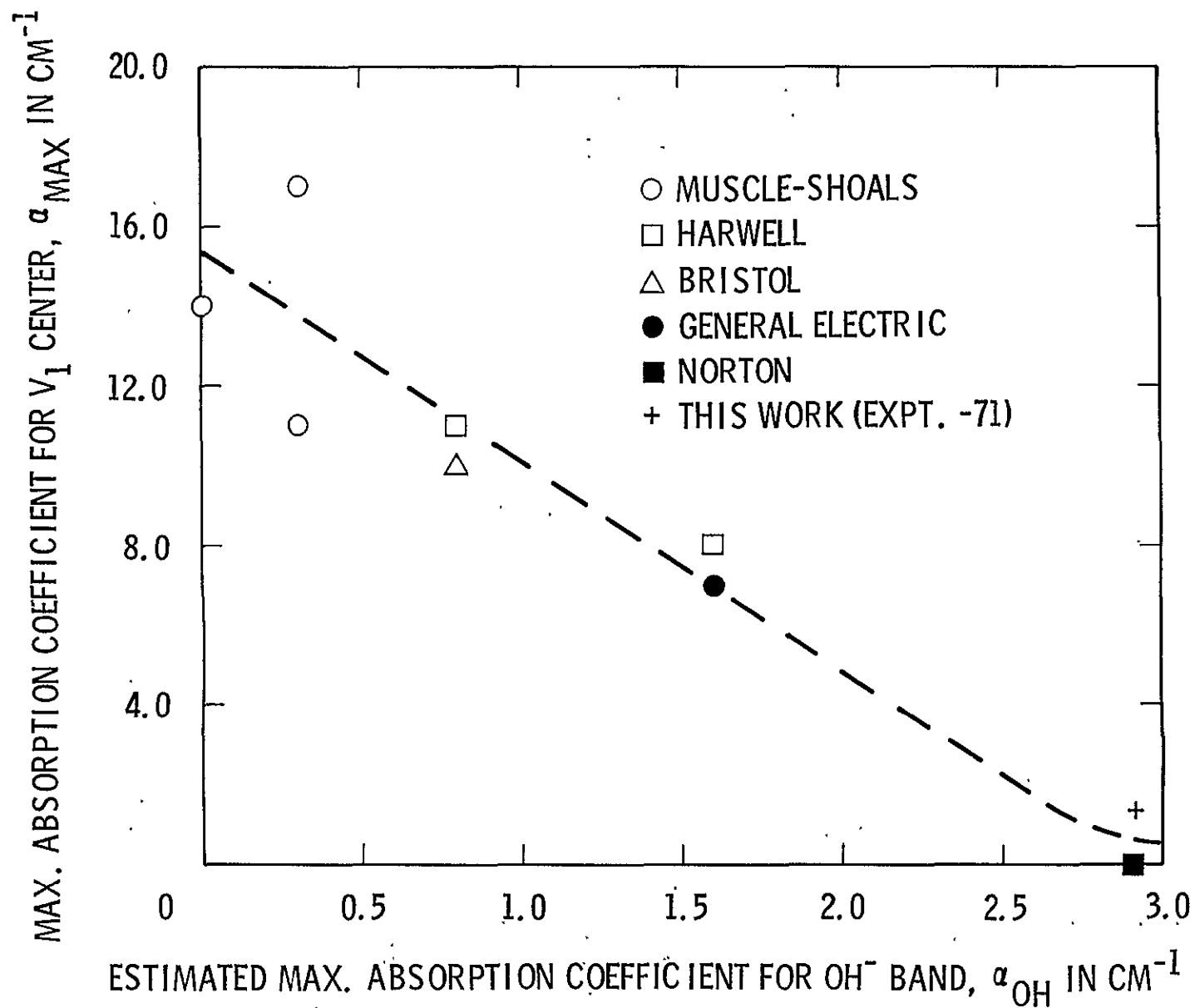


Figure 6. Chen and Sibley² data for γ -radiation induced maximum V_1 center absorption as a function OH^- content in MgO single crystals from various sources

There is limited substitutional solubility of V^{3+}/V^{2+} (not of V^{5+})⁶ but no indication of being of real importance to radiation induced defect kinetics. The divalent ions of Ni and Cu also appear to have limited solubility in the MgO lattice but no apparent importance to radiative coloration. Note that the preferred valence state of the iron and titanium are subject to thermal history. Thus for the region of impurity levels shown in Table 1, oxidation at 1200-1500°C favors the states Fe^{3+} and Ti^{4+} , while reduction (in vacuum, inert gas, or hydrogen) at 1200-1500°C favors Fe^{2+} and Ti^{3+} . In terms of iron, such partition of valence states by means of thermal treatment and environment control is illustrated by the following experimental data (Table 2) on both low and high purity single crystal MgO.

Table 2. Processing Effects on Fe^{3+}/Fe^{2+} Distribution in Single Crystal MgO

Process	Ions */cm ³	
	Fe^{3+}	Fe^{2+}
<u>Low Purity Crystal</u>		
As received (expt. -50)-----	4.8×10^{18}	0.0
Soak at ~1450°C in N ₂ for 4 hrs. followed by intermediate cooling rate $\approx 25^\circ\text{C}/\text{min}$ (expt. -66)---	0.02×10^{18}	4.2×10^{18}
<u>High Purity Crystal</u>		
As received (expt. -55)---	2.0×10^{17}	0.7×10^{17}
Soak at ~1450°C in N ₂ for 4 hrs. followed by intermediate cooling rate $\approx 25^\circ\text{C}/\text{min}$. (expt. -63)---	0.4×10^{17}	5.4×10^{17}
* Fe^{1+} not considered present. The variation in total iron content ($Fe^{2+} + Fe^{3+}$) observed for a <u>given material</u> results from (a) contamination during processing, (b) errors in instrumental analysis, and (c) concentration variations within a single ingot.		

The ions Cr^{3+} , Mn^{2+} , and Co^{2+} are typically not affected by such crystal treatment.

2.4.3 Alkali Metal Cations

Adam and Brindley⁶ investigated a range of monovalent, divalent, trivalent, tetravalent, and pentavalent cation and cation pair solutions in crystalline MgO . The $\text{Li}^{1+}\text{-Al}^{3+}$ pair was reasonably soluble but the $\text{Na}^{1+}\text{-Al}^{3+}$ pair was not. $\text{Li}^{1+}\text{-Cr}^{3+}$, $\text{Li}^{1+}\text{-Mn}^{3+}$, $\text{Li}^{1+}\text{-Fe}^{3+}$, and $\text{Li}^{1+}\text{-Ti}^{4+}$ pairs were also quite soluble. The $\text{Li}^{1+}\text{-V}^{5+}$ and $\text{Li}^{1+}\text{-Mn}^{4+}$ pairs were not. From their data it seems reasonable to assume that, of the alkali metal ions, only Li^{1+} provides cation charge compensation in the lattice for substitutional ions of valence greater than 2+. The importance of such charge compensation may be understood by recognizing that for each two trivalent cations (e.g., Fe^{3+}) which are not compensated a $\text{V}_{\text{Mg}}^{\prime\prime}$ is generated. This $\text{V}_{\text{Mg}}^{\prime\prime}$ is a potential hole trap.

2.4.4 Miscellaneous Cations

Lattice effects of Al^{3+} , Si^{4+} , P^{3+} , and B^{3+} , either in substitutional or interstitial positions, are not yet sufficiently understood to gauge their role in regulating radiative coloration processes. However, it is not unreasonable to suspect that Al^{3+} , for example, might participate as an electron trap or as a recombination center.

2.4.5 Anion Impurities

Trivalent, substitutional anions (e.g., N^{3-}) can generate $\text{V}_{\text{O}}^{\cdot\cdot}$; while monovalent anions (e.g., F^{1-}) can oppose such oxygen vacancy generation. In addition to generation of trapping sites, each may participate directly as a defect state. Thus the V_{F} center has been reported⁴ to consist of: $\text{F}^{-}\text{-V}_{\text{Mg}}^{\prime\prime}\text{-O}^{-}$. This center is observed to be the analog of the V_{OH} center.

Nothing is known of defect states involving nitrogen ions.

2.4.6 Fe^{3+} -Doping Procedure

Selective doping of Fe^{3+} into a high purity MgO lattice offers the potential for:

- a. An increase in the concentration of Mg^{2+} vacancies, $[\text{V}_{\text{Mg}}'']$, provided it is not accompanied by an increase in Li^+ concentration.
- b. Controlled introduction of a recombination center and a carrier trap at the same time. The nature of the trap appears to be a function of the level of the doping, net electron trapping being associated with $[\text{Fe}^{3+}]_0 \geq \sim 4 \times 10^{18}/\text{cm}^3$. Net hole trapping seems to occur below this Fe^{3+} level with the impurity matrices shown in Table 1.

A thermal diffusion procedure was developed for this doping. The first step consisted of thermal vaporization of high purity iron (6-9's purity) at 10^{-5} torr on to freshly cleaved specimen wafers of high purity MgO (0.75-1 mm thick). Coating thicknesses of the order of 2500 Å were used for high level doping. Lower iron doping levels would require commensurately thinner coatings. These crystals were stored in a dessicator until packaged for use just prior to thermal treatment.

Packaging for thermal treatment was designed to minimize impurity contamination from the high temperature ambient. Working in a "clean cabinet" the specimen crystal wafers were first enclosed in a platinum foil capsule measuring 3/8 inch O.D. x 1 inch (0.0005 inch foil thickness). This first capsule was then enclosed in a second slightly larger Pt foil capsule. This package was next immersed in high purity MgO powder contained in a 3/4 inch O.D. x 1-5/8 inch Pt container and then covered. This final package was loaded into a MgO crucible (Leco Number 528-701, 99.5 percent wt. MgO typical, 1-1/4 inch O.D. x 1-3/4 inch) fired to 1500°C prior to use.

Immediately before carrying out the diffusion experiment, the loaded MgO crucible was transferred from a desiccator to a graphite susceptor (baked out at 110°C for 24 hours), covered with a graphite lid containing a pyrometer view port, and placed in an induction furnace with rotary pedestal (Futurecraft). The system was closed and carefully purged with dried N₂ gas. Continuing this inert gas purge, the temperature of the Pt package was raised to ~1460°C in approximately one hour. A temperature of 1460-1480°C was maintained for nine hours, at which time the crystal package was rapidly cooled to <500°C at an initial rate of ~6°C/sec which then decreased to ~2.5°C/sec. The cooled, loaded MgO crucible was quickly transferred from the induction furnace to a desiccator and taken to a clean cabinet. Here, the entire MgO crucible was wrapped in 0.5 mil Pt foil.

This latter package was next placed in a globar furnace (SiC elements) for selective oxidation of the iron introduced into the lattice. Employing an air ambient, the temperature was raised to ~1480°C within about five hours. After soaking at this temperature for four hours, the hot MgO crucible was quickly removed from the furnace and air-quenched on a heavy aluminum plate (cooling rate ≈ 10°C/sec initially, dropping to ~2.5°C/sec at 500°C).

Table 3 indicates the effectiveness of this doping procedure and is based on optical, EPR and spectrographic analyses.

Table 3. Fe³⁺-Doping of High Purity Single Crystal MgO

Process	Ions [*] /cm ³	
	Fe ³⁺	Fe ²⁺
Undoped (-55)	2. x 10 ¹⁷	0.7 x 10 ¹⁷
Fe ³⁺ -Doped (-67)	1.5 x 10 ¹⁹	4.3 x 10 ¹⁹
*Fe ¹⁺ not considered		

The Fe^{3+} content is noted to have been increased two orders of magnitude. Reference to appropriate experiment numbers (in parentheses) in Table 1 indicates that this increase was accomplished with little significant contamination. An increase in the $[\text{Fe}^{3+}]$ relative to the $[\text{Fe}^{2+}]$ in the doped specimen can be effected by a longer soaking period during oxidation.

Uniformity of bulk distribution was not determined. This is an important consideration. However, careful visual examination of the doped crystals revealed a uniform yellow coloration, excellent transparency (except for a minor number of striae initially present), no cloudiness, and no obvious clustering or other irregularities. While not conclusive, such cursory examination seemed to preclude the need during this phase of the effort for more sophisticated examination of doping uniformity, e.g., by means of direct imaging mass analysis.

3.0 COLOR CENTER GENERATION IN MgO

In addition to several preliminary experiments with MgO powder to permit check-out of irradiation and detection facilities, a total of seven, radiative coloration experiments were performed. Each was continuous, ranging in duration from 6 to 12 days. All were conducted at room temperature in a vacuum of $\sim 10^{-8}$ torr backfilled to 10^{-5} torr with high purity H_2 gas (Matheson Co., 99.9995 percent vol.). Proton energy was maintained at 1.0 keV in all cases. Proton flux was varied over the range 3×10^{11} to 4×10^{11} $p^+/\text{cm}^2\text{-sec}$. Depending on which value is accepted for the solar wind proton flux, experimental proton irradiations were carried out at rates of the order of 1000-1500 \times solar. In parallel, an ~ 1 eV electron (e^-) beam (non-luminous in the visible wavelengths) was directed at the target at an intensity slightly greater than that of the proton beam. Flux values were controlled within the limits of $\sim \pm 10$ percent. Reflectance changes were measured as often as once/day or as otherwise deemed necessary to monitor the color changes produced. Upon termination of an experiment, corresponding reflectance and EPR spectra were obtained.

3.1 POWDER EXPERIMENTS

The first experiment was conducted with powder. An impure material (reagent grade, see Table 1) was selected deliberately and compressed into chips, without subsequent thermal annealing, to further increase the defect structure. Irradiation of such material was expected to provide a broad spectral look at the distribution of impurities one might encounter under worst conditions. Such examination might then suggest means of keeping the problem tractable and yet confined only to those areas pertinent to solar thermal control.

The absorption change generated by a total proton fluence of 2.6×10^{17} p^+/cm^2 is shown in Figure 7. Estimated Gaussian resolution (see Appendix A) of the overall spectrum into component spectra

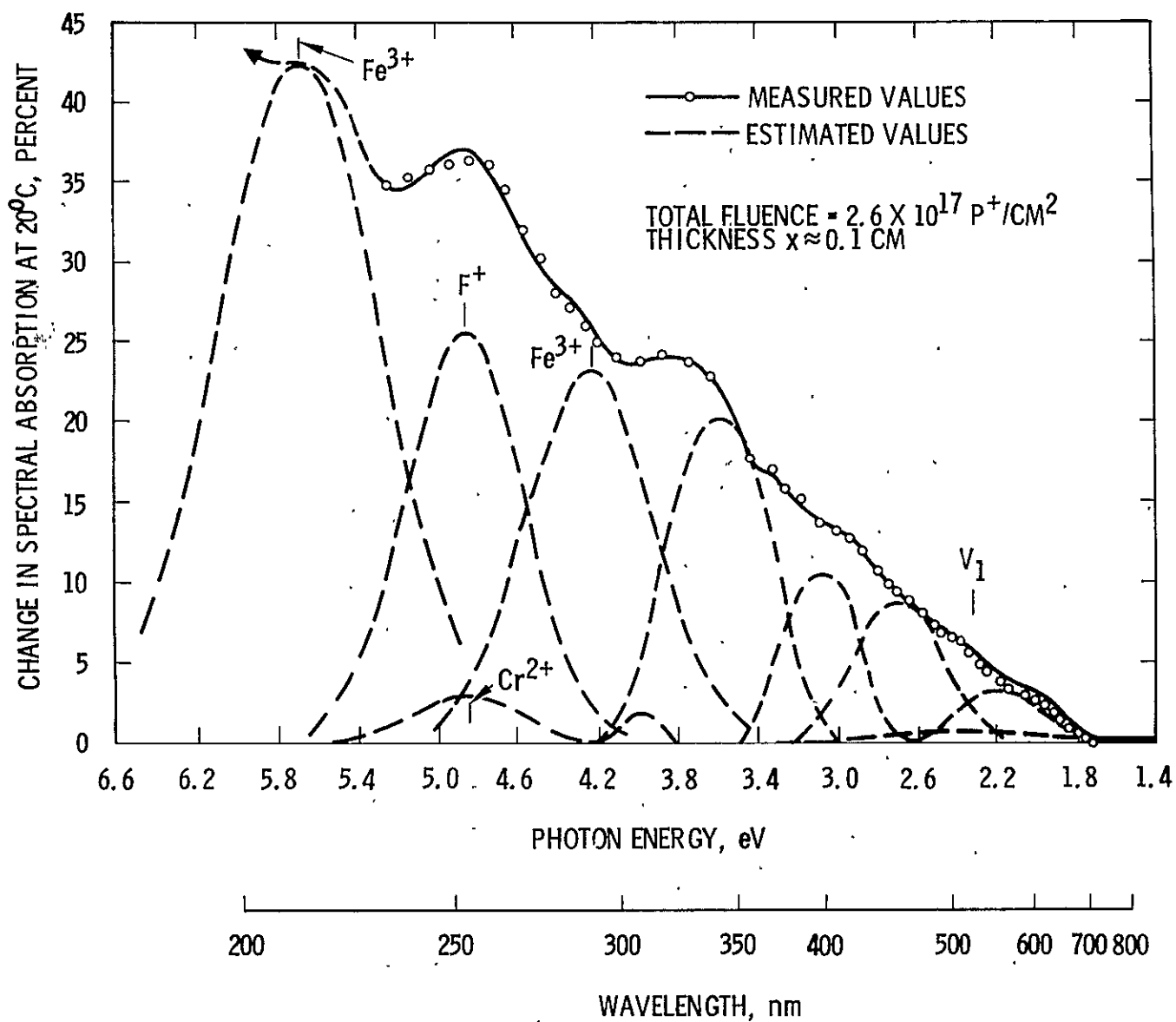


Figure 7. Absorption change in MgO powder (compressed) induced by a 1.0 keV neutralized proton beam at 20°C and 10^{-5} torr H_2 (F1799-43)

is indicated. The F^+ -center and Cr^{3+} spectra are only approximate. The importance of this experiment was to point out the following:

- a. The major portion of the coloration even in a very impure dielectric, is displayed in the near-UV.
- b. Component resolution at photon energies ($h\nu$) greater than ~ 5.0 eV is seriously handicapped (if not impossible) at this time because of the lack of model information of resonant color centers in this region. Henderson, King, and Stoneham⁷ have made tentative suggestions in this regard.
- c. A number of unidentified spectra are displayed at the photon energies corresponding to the visible wavelength region. These overlap the identified V_1 center. Since the resolution of the V_1 band is important to the attempt to study defect kinetics, reduction of adjacent overlapping band structure might be attempted by resort to higher purity materials. Additionally, since EPR powder spectra are more complex than those for the single crystal, attention was further directed toward higher purity single crystals for subsequent experiments.
- d. As far as near-infrared defect display is concerned, little was observed. Many workers have reported a band at 1.2 eV (1.03μ), and Henderson and Wertz have noted that it changes in concert with the 3.6 eV band. This band was not observed in this work. Small initial bands at ~ 1.55 eV (0.8μ) and ~ 0.9 eV (1.38μ) were observed regularly, but were unchanged by irradiation. These are likely associated with free water and/or CO_2 .

3.2 SINGLE CRYSTAL EXPERIMENTS

3.2.1 Effect of Controlled Chemical Processing

A primary consideration to color center experimentation is the defect structure (both intrinsic and extrinsic) resulting from initial preparation and as modified by post-processing. This matter has

been discussed earlier but is such a dominant consideration as to warrant both restatement and illustration. Present limitations in defect modeling and precise characterization techniques limit the guidance available to preparatory efforts. Thus, (a) careful planning within the context of available data and (b) very careful handling procedures are an absolute requirement. Illustrative of item (a) is the previous discussion of the possible effect of OH^- concentration on the radiation-induced density of the V_1 center which absorbs solar energy near the peak of the solar spectrum. The presence of OH^- appears to suppress V_1 center formation by favoring V_{OH} center formation, the latter absorbing optical energy is a narrow band centered at 3.0μ (i. e. outside the solar region). Recognizing that other factors might also enter, at least the option of introducing OH^- (say by starting with purified $\text{Mg}(\text{OH}_2)$ in order to suppress radiative formation of V_1 centers should be considered prior to material preparation.

Care in material handling, the second item above, as well as the option of post-preparatory processing are well illustrated by Figures 8, 9, and 10. The crystals used for the two experiments involved (-55, and -63) were all cleaved from a single, small section within one high purity ingot. Careful reduction (and annealing), as indicated partly by little increase in impurities in Table 1, is demonstrated by comparison of Figures 9 and 10. Note that the processed material was subjected to over twice the proton fluence imposed on the as-received material. Despite this, radiative-induced optical absorption in the near-UV is reduced by a factor ranging from 1/3 to 1/10. Thus, chemical reduction of the iron 3+ state, without attendant contamination or other deleterious effects, contributes by decreasing radiative coloration over broad regions centered at 4.25 eV and 5.7 eV (the latter Fe^{3+} band not being shown). The 3.6 eV band, although not yet identified, is considered by Hansler and Segelken⁸ to represent absorption by a center consisting of an electron trapped at an intrinsic lattice defect. Comparison of Figures 9 and 10 would indicate that this defect was effectively

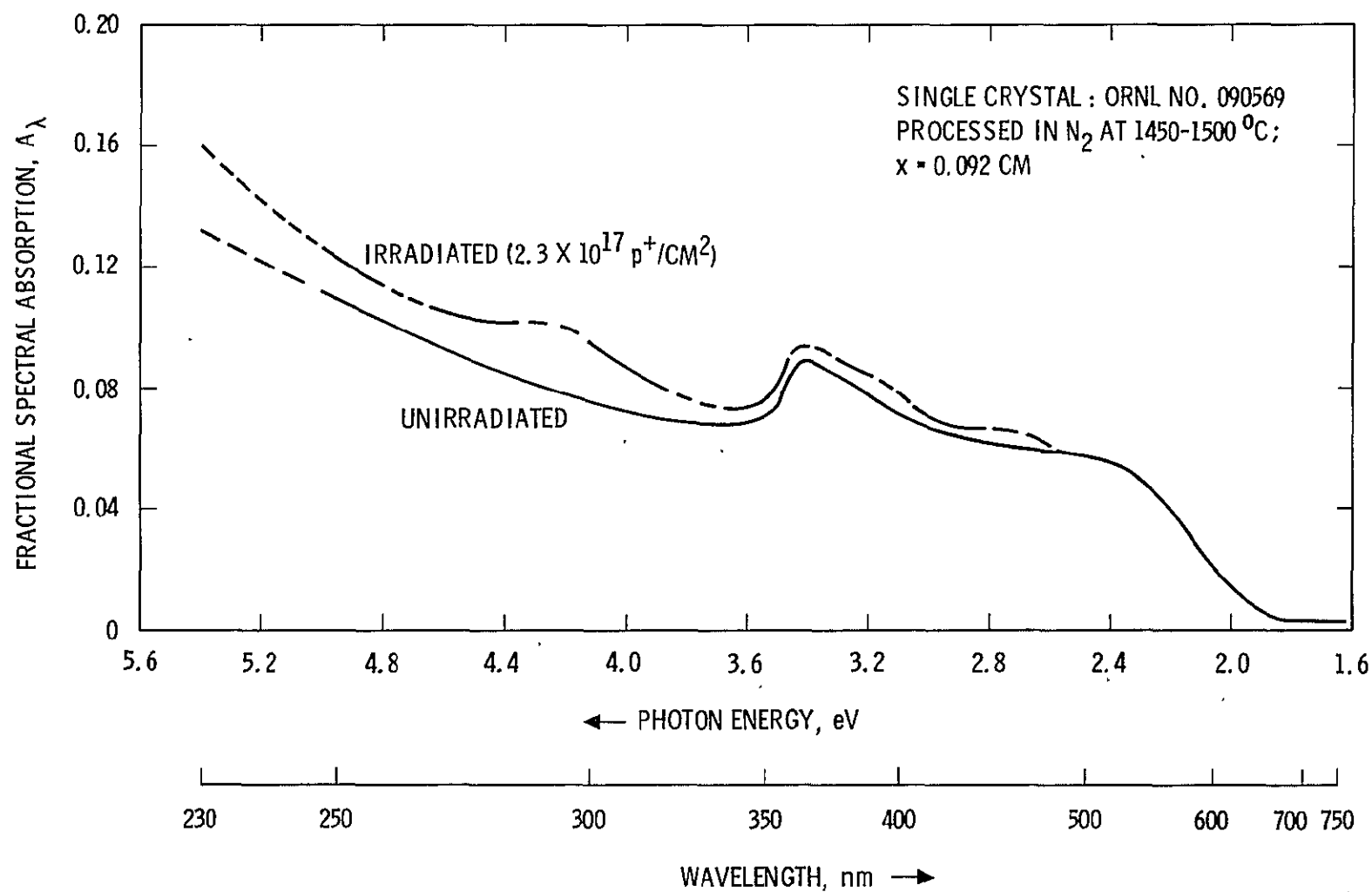


Figure 8. Change in optical absorption induced in processed, high purity MgO single crystal by neutralized 1.0 keV proton beam at 20 $^\circ\text{C}$ and 10^{-5} torr H_2 (F1799-63)

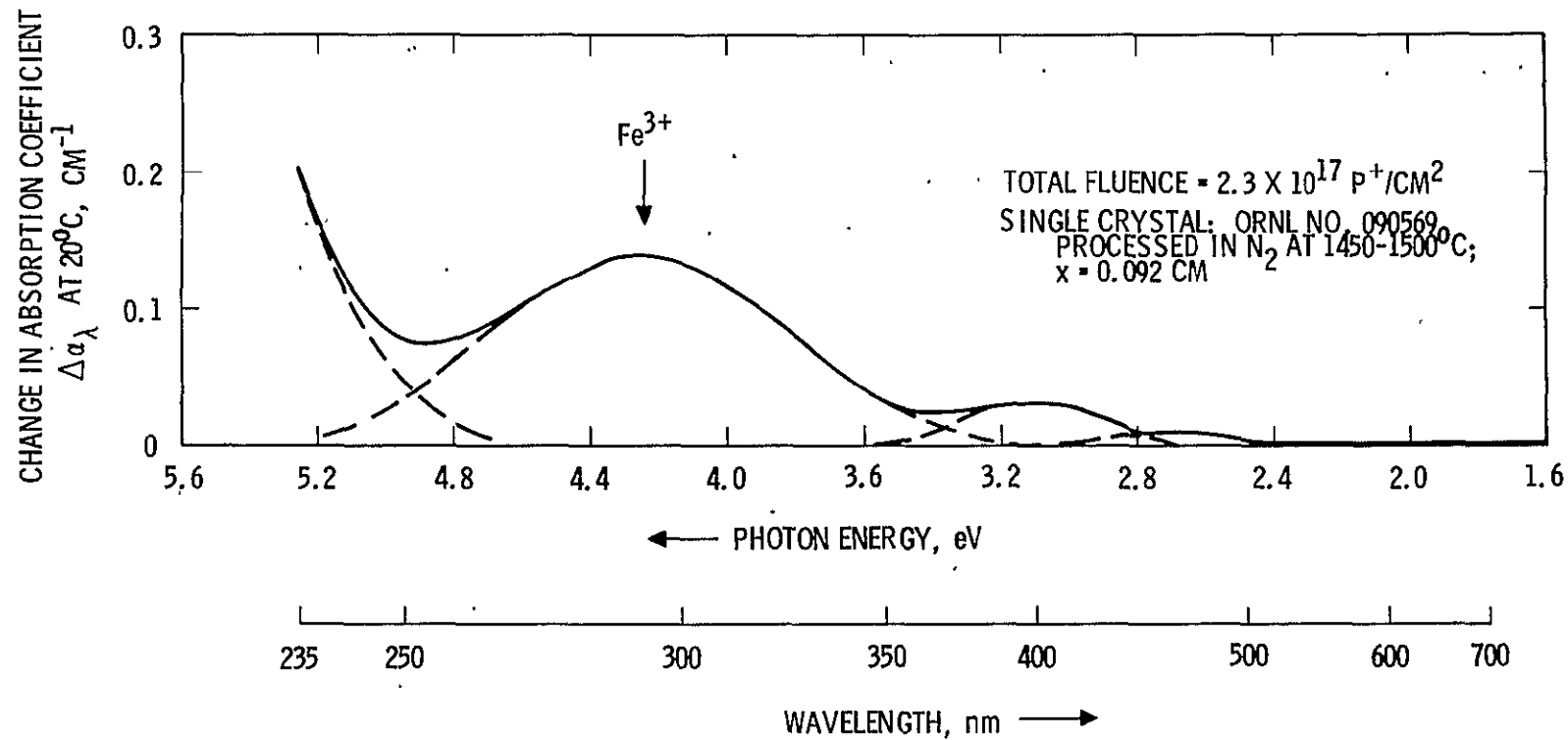


Figure 9. Change in spectral absorption coefficient induced in high purity MgO single crystal by neutralized 1.0 keV proton beam at 20°C and 10^{-5} torr H₂ (F1799-63).

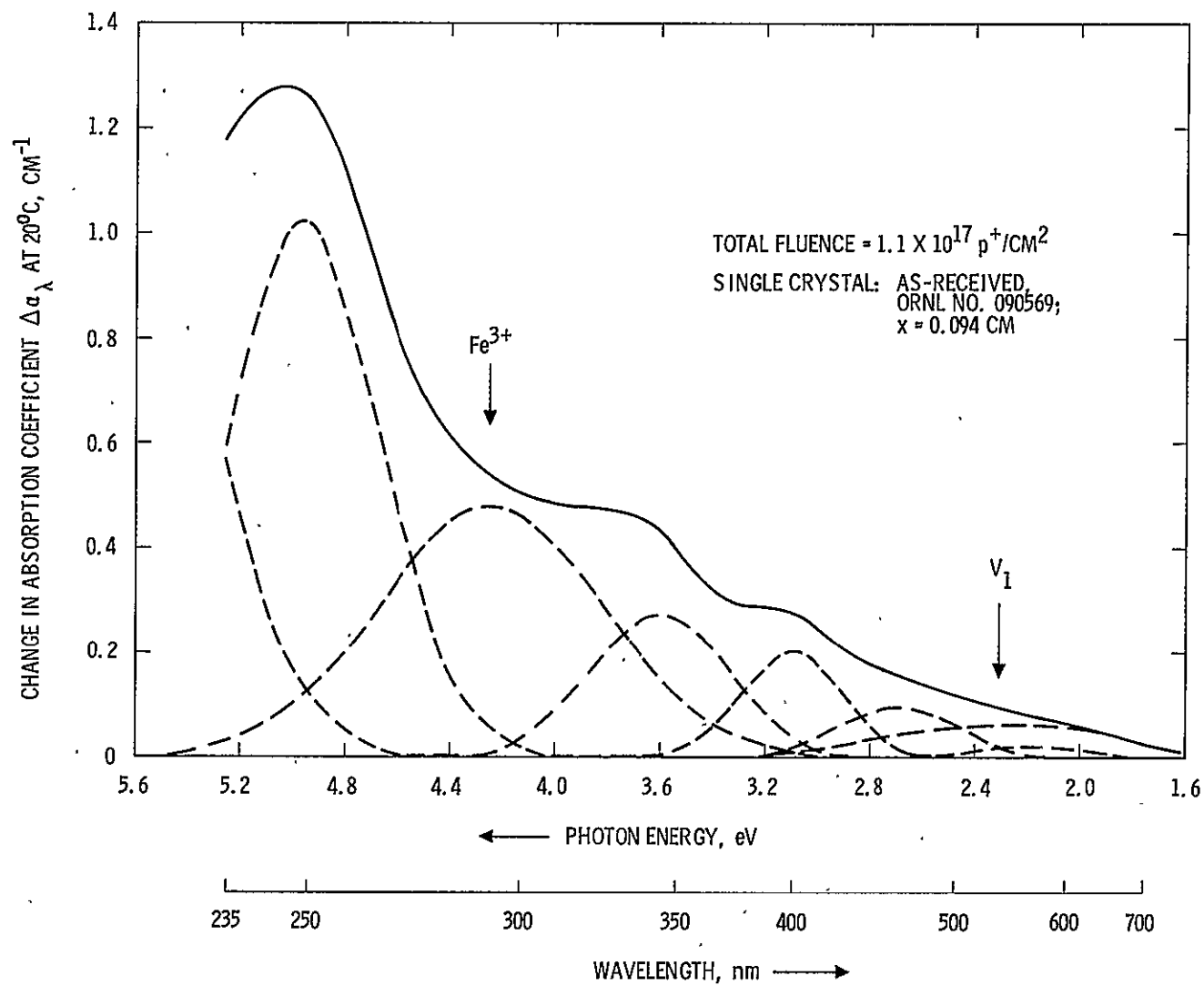


Figure 10. Change in spectral absorption coefficient induced in high purity MgO single crystal by neutralized 1.0 keV proton beam at 20°C and 10^{-5} torr H₂ (F1799-55)

removed by annealing as a result of processing at 1450-1500°C in nitrogen gas. Other, unidentified near-UV bands, either generated or which grow during p^+ -irradiation, are seen to be similarly reduced as a result of such controlled chemical processing.

Similar decrease in spectral absorption in the visible region is also noted. The V_1 center which requires a density of V''_{Mg} was not observed in the processed crystals. This fact indicates that the $[V''_{Mg}]_0$, i.e. prior to irradiation, was negligible and results from a minimized $[Fe^{3+}]_0$ and unidentified annealing effects. The effect of p^+ -generated V''_{Mg} in the proton range is discussed later.

As mentioned earlier, negligible radiative coloration was observed in the near-IR. This was true even in the case of very impure, highly stressed materials.

Please note that the absorption coefficients which are referred to in the above figures are not true absorption coefficients. That is, they do not represent a uniform coloration of the bulk thickness. This results from proton stopping in the surface layer and subsequent charge carrier diffusion into the bulk to some undetermined distance less than the specimen thickness. Thus the $\Delta\alpha_\lambda$ values represent a mean value over the total crystal thickness. Since crystal thicknesses varied among experiments only $\pm 10\%$, such values provide a useful basis for comparing defect spectra.

3.2.2 Effect of Selected Impurities

3.2.2.1 Iron. Comparison of the crystals used in experiments -63 and -66 on an impurity basis only (see Table 1) reveals one major variation, namely the total iron content. Both were processed simultaneously; after which the $[total\ Fe]_{-66} \approx \frac{7}{8} [total\ Fe]_{-63}$. Processing was designed to minimize the initial density of the 3+ state of iron and anneal out some of the intrinsic defect structure. Comparison of the optical absorption spectra for the unirradiated specimens (see Figures 8 and 11) indicates considerable similarity. Only after comparable proton irradiance ($>10^{17}\ p^+ / cm^2$) does the difference between the relatively pure (low iron content) and the impure (high iron content)

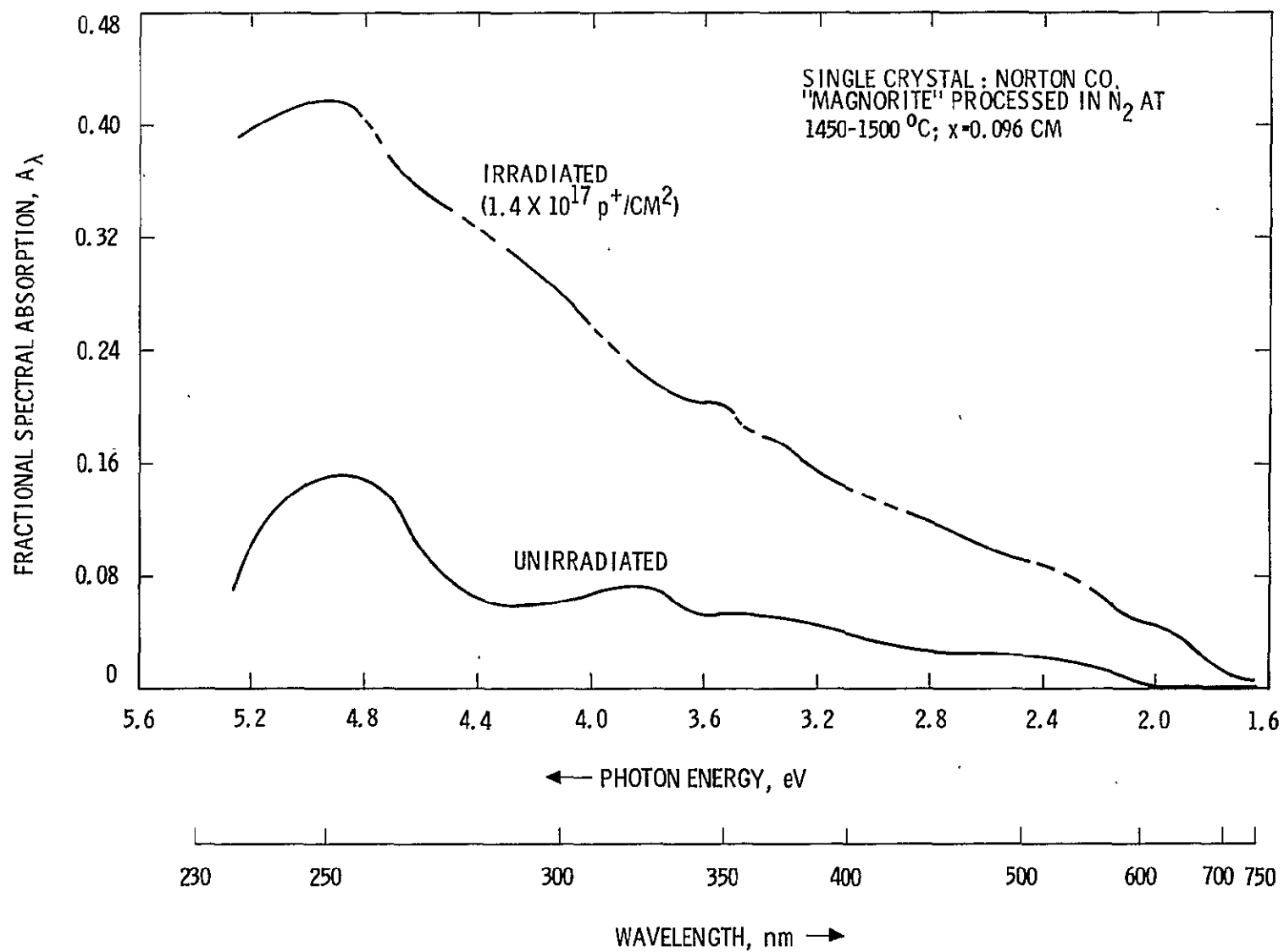


Figure 11. Change in optical absorption induced in low purity MgO single crystal by a neutralized 1.0 keV proton beam at 20°C and 10^{-5} torr H₂ (F1799-66)

crystals manifest itself. Thus proton irradiation increases the solar absorptance α_S (see Blair⁹ for spectral weighting factors) of the pure crystal an order of <5% from ~ 0.03 to ~ 0.031 . Compare this to an increase of the order 200% for the impure crystal, from ~ 0.025 to ~ 0.075 , for an even lower proton fluence.

The reasons for this divergence may be observed by comparing component defect spectra (see Appendix A for basis of Gaussian resolution technique) shown in Figures 9 and 12. In the low purity crystal, certain features are obvious as follows:

- a. Growth of the Fe^{3+} bands (i.e. resulting from net h^+ -trapping by Fe^{2+} recombination centers).
- b. Filling of intrinsic, electron traps, e.g. by V_O and yielding absorption near 5.0 eV (F^+ and F^- centers) and by absorption centered at 3.6 eV.
- c. Filling of intrinsic, hole traps, e.g. by V_{Mg}'' and yielding absorption centered at 2.3 eV (V_1 center).

In the case of the high purity crystal, all of the above are suppressed to varying degree.

Selective doping with iron to a relatively high density can also suppress radiation-induced defect density. Regardless of processing, both $[\text{Fe}^{3+}]_0$ and $[\text{Fe}^{2+}]_0$ are so large that, acting as recombination centers, they are able to suppress trapping of proton-generated charge carriers, both e^- and h^+ . Thus proton-induced coloration is small. Such high level Fe-doping is indicated in Table 1, noting that the total iron content of crystals in experiment (-67) was increased to $\sim 100 \times$ that of the crystals in experiment (-55), other impurity concentrations remaining about the same. The penalty associated with such bulk-suppression, in terms of thermal control, is very broad, initial, UV absorption tailing strongly into the visible region. This Fe^{3+} - related absorption would not prove acceptable in a thermal control application. Because at densities of 5.8×10^{19} total Fe/cm^3 ($= 541$ ppma), the $\text{Fe}^{3+}/\text{Fe}^{2+}$ densities dominate the electronic processes, this material did not prove too useful in studying defect kinetics. In concluding, note that Haxby¹⁰ also observed this effect of iron-doping (0.01 to 0.40% wt.)

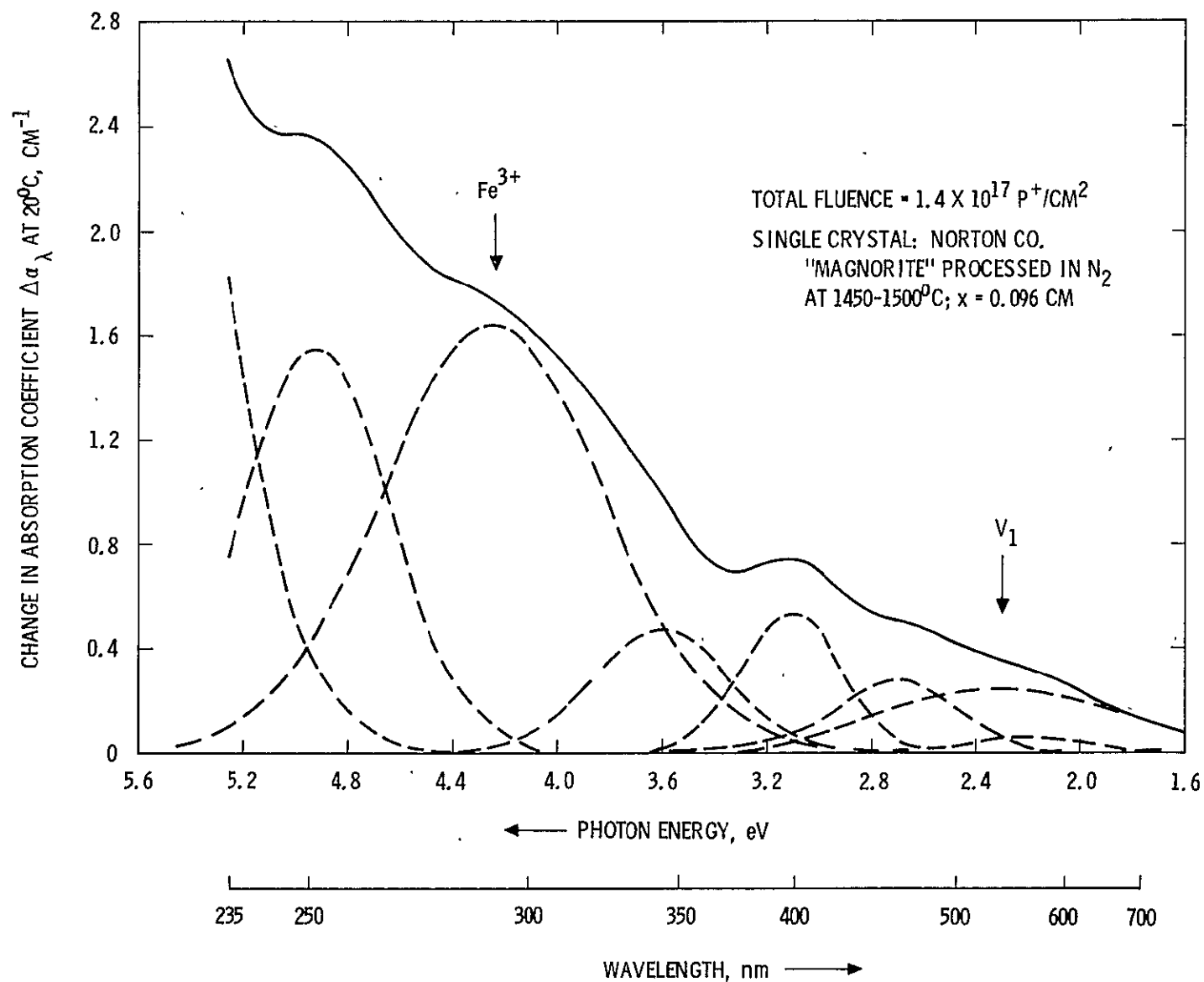


Figure 12. Change in spectral absorption coefficient induced in low purity MgO single crystal by a neutralized 1.0 keV proton beam at 20°C and 10^{-5} torr H₂ (F1799-66)

in regard to color center suppression (in the bulk) during X-irradiation of MgO single crystals (compare his Figures 3 and 10).

3.2.2.2 Hydrogen as OH⁻. A broad, near-IR band centered near a wave number of 3400 cm^{-1} ($\lambda = 2.94\mu$) has been associated⁴ with substitutional OH⁻ in isolated sites. Glass and Searle¹¹ have also attributed a nearby band (at 3700 cm^{-1}) to Mg(OH)₂ precipitates in MgO.

Optically resonant associated (or aggregate) centers formed by adjacent V_{Mg}^{''} - OH⁻ pairs with an adjacent trapped h[•] have been discussed earlier in Section 2.4.1. They are discussed further in Section 3.3 in terms of the EPR work. Neither these aggregate centers nor the isolated OH⁻ center were examined by optical spectroscopy during this work. However, they appear to be of importance.

Two important conclusions derive from the above discussed data as follows:

- a. The term purity must be considered in a very selective manner and is only relevant to the problem of radiative coloration when employed in the context of a given crystal lattice.
- b. Despite current gaps in color center knowledge, this body of information can be introduced into preparatory and (post-processing procedures in order to suppress radiative coloration of a dielectric, e.g. MgO. Preliminary application of such understanding toward development of a radiation-stable pigment for spacecraft thermal control is illustrated quite well by Figure 8.

3.3 POINT DEFECT IDENTIFICATION BY SPIN RESONANCE

Electron paramagnetic resonance (EPR) measurements were carried out on the crystal specimens to provide supplementary defect identification and measurement for the optical data. EPR measurements were only possible after experiment termination. They were arranged so as to prevent post-experiment optical and/or thermal bleaching. Thus EPR measurements and terminal optical spectra are

considered to correspond, both being made in-situ (vacuum). Handicapping these EPR measurements were such factors as the following:

- Microwave power saturation of selective defects, e.g. F^+ .
- Orientation problems associated with various anisotropic centers, e.g. Fe^{3+} and the various V-centers.
- Errors introduced into defect density calculations because of poorly defined spectra, especially spectral tails.
- The presence of defects with overlapping spectra, making resolution of components difficult and subject to error.
- Inability to display certain potentially observable valence states satisfactorily except at 4°K (e.g. Fe^+) and others not at all (e.g. Fe^{2+}).

These and other problems serve to limit the potential usefulness of the EPR spectra. Despite such shortcomings, these data did serve as a valuable supplement to the optical measurements.

Defect densities calculated from typical EPR measurements are compared below with results derived from corresponding optical measurements (see Table 4).

Table 4. Selected Defect Determinations Obtained From Corresponding EPR and Optical Data

		Defect Density, $10^{17}/\text{cm}^3$			
		Fe^{3+}	Fe^{2+*}	V_I	Cr^{3+}
<u>Experiment (-50)</u>					
Optical	Unirrad.	48.0	0.0	0.0 (est.)	nd
	p^+ -irrad.	34.0	14.0	0.2	nd
EPR	Unirrad.	54.0	0.0	nd	13.0
	p^+ -irrad.	31.0	23.0	nd	11.0
<u>Experiment (-71)</u>					
Optical	Unirrad.	4.6	4.1	0.0 (est.)	nd
	p^+ -irrad.	6.4	2.3	0.2	nd
EPR	Unirrad.	--	--	nd	3.
	p^+ -irrad.	--	--	nd	3.
	γ -irrad. (satn.)	0.7	8.0	0.8	0.7
*Obtained by subtracting Fe^{3+} from total iron density.					
nd - not detected					

As indicated by these typical data, EPR and optical results were generally consistent.

Gamma radiation (in vacuum) of corresponding crystal specimens were frequently carried out to examine bulk saturation effects. Typical dose was 15 Mrad of 1 MeV γ -radiation. The γ -induced EPR spectrum may be compared in Figure 13 with the spectrum of the unirradiated specimen used in experiment (-71). The region covered ranges from a low field side of $H = 3254.94$ gauss ($g = 2.0383$) to a high field side of 3351.40 gauss ($g = 1.9796$) in the direction shown. The following defect density values attained at saturation by ionizing radiation were estimated from component V_{OH} , V_F , and V_1 spectra in Figure 13 as follows:

$$[V_{OH}] \approx 3.53 \times 10^{17} / \text{cm}^3$$

$$[V_1] \approx 0.79 \times 10^{17} / \text{cm}^3$$

$$[V_F] \approx 0.32 \times 10^{17} / \text{cm}^3$$

$$\text{Total} \approx 4.6 \times 10^{17} / \text{cm}^3$$

These data provide information pertinent to defect studies in the following manner:

- a. Comparison between $[V_1]$ generated by p^+ - and by γ -irradiation indicates the approach to saturation in regard to this center, i.e. 25 percent in this case.
- b. Based only on impurity-introduced cation vacancies, one may estimate $[V_{Mg}]_0$ as an order of $10 \times 10^{17} / \text{cm}^3$. Mg^{2+} vacancies introduced thermally (as during preparation) would add to this value of course. In any event, one would expect a significant portion of these

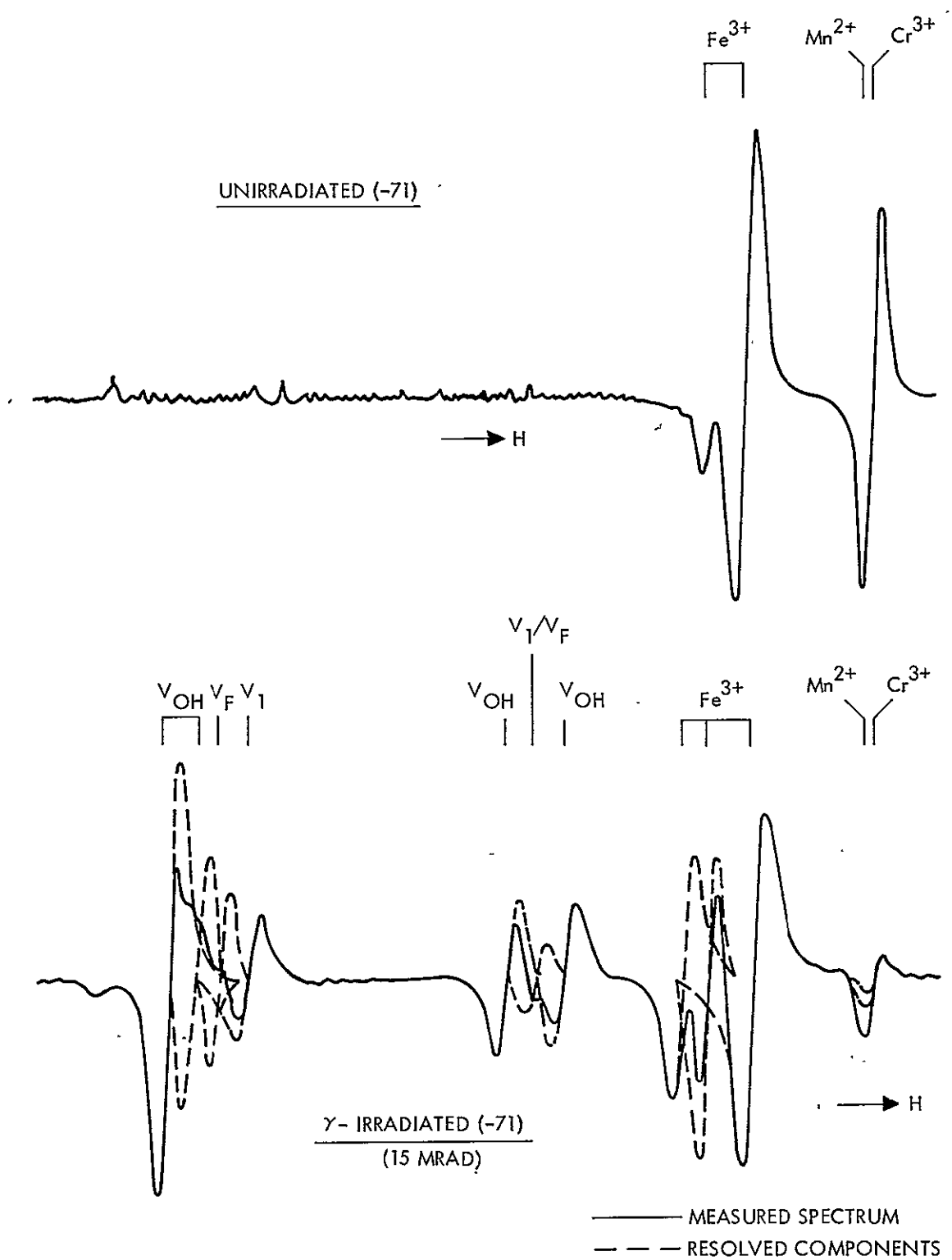


Figure 13. Effect of gamma-irradiation (in vacuum at 20°C) on EPR spectra (79°K) of air-quenched, moderate purity, single crystal MgO

vacancies to become converted to V-centers as a consequence of h⁺-trapping during γ-irradiation. In this regard compare the saturation density of V-centers (measured by EPR above $\approx 4.6 \times 10^{17}/\text{cm}^3$) with the Mg^{2+} vacancy density of $\sim 10.0 \times 10^{17}/\text{cm}^3$.

- c. By means of the Smakula-Dexter equation relating defect density with optical resonance, one may estimate $(\alpha_{V_1})_{\text{max}}$. Separate estimation of α_{OH} allows comparison with the data in Figure 6. Thus:

$$N = S \cdot \alpha_{\text{max}}$$

where

$$N = \text{defect density, no.}/\text{cm}^3$$

$$S = \text{Smakula-Dexter band constant} = 6.4 \times 10^{16} \text{ cm}^{-2} \text{ for } V_1 \text{ center}$$

$$\alpha_{\text{max}} = \text{absorption constant at band peak, cm}^{-1}$$

From above, using data presented earlier and in Appendix A:

$$(\alpha_{V_1})_{\text{max}} = \frac{0.79 \times 10^{17}}{6.4 \times 10^{16}} = 1.2 \text{ cm}^{-1}$$

Approximate $[\text{OH}^-]$ in MgO by an expression given by Kats¹⁷ for $[\text{OH}^-]$ in quartz crystal as follows:

$$N_{\text{OH}^-} = 6.32 \times 10^{17} (\alpha_{\text{OH}})_{\text{max}}$$

Further, estimate that $N_{\text{OH}^-} \approx 5 \left[V_{\text{OH centers}} \right] \approx 5 \times 3.53 \times 10^{17} / \text{cm}^3$.

$$\left[\alpha_{\text{OH}} \right]_{\text{max}} \approx \frac{5 \times 3.53 \times 10^{17}}{6.32 \times 10^{17}} \approx 2.7 \text{ cm}^{-1}$$

These corresponding maximum values of α_{V_1} and α_{OH} are plotted in Figure 6 and show reasonable agreement.

In EPR work, the detection threshold is typically a direct function of absorption signal half width. The detection threshold for the EPR system used is estimated as 5×10^{14} spins. On the basis of the typical sample volume $\approx 0.1 \text{ cm}^3$, a detection threshold of an order of 5×10^{15} defects/ cm^3 , MgO is thus established for defects displaying relatively narrow lines, e.g. Cr^{3+} in cubic symmetry. It was found that broader lines, e.g. Fe^{3+} , could not be observed below an order of $5 \times 10^{16} \text{ Fe}^{3+} / \text{cm}^3 \text{ MgO}$.

4.0 COLOR CENTER GENERATION KINETICS IN MgO

Theoretical studies¹² performed during the first year of this effort indicated that defect kinetics associated with low energy protons (in dielectric targets of thickness \gg proton range R_p) were regulated by proton-generated lattice displacement within a "surface" layer defined by R_p . Thus in the case of MgO, the V_1 center density $[V'_{Mg}]$, deemed important because of its optical resonance in the visible spectrum, was indicated to track the density of magnesium ion vacancies $[V''_{Mg}]$ primarily determined by time-integrated proton dose. Steady state or saturation defect densities were expected when high probability, $V''_{Mg} - Mg_i$ pair separation was attained as a result of irradiation. Estimates of such Frenkel pair separation led to expected, saturation, defect densities approaching $2.7 \times 10^{21}/\text{cm}^3$ as a limit. It was appreciated that charge exchange processes involving impurities were important in terms of their function as individual color centers. In the case of dielectrics these centers typically display near-UV absorption and are thus of minor importance to solar absorption. It was believed the primary role of substitutionally soluble impurities was to participate in regulating the available density of holes (h^\cdot) or electrons (e^\cdot) at any time t . The alternate or indirect role of impurities, e. g. in establishing initial densities of lattice vacancies, seemed unimportant when compared to the effect of stopping keV protons. The following premises thus seemed reasonable as a guide for initial experiments:

- (a) Proton damage restricted to a surface layer of the order of 10^{-6} cm (100 Å).
- (b) Measured radiative coloration sensitive only to selective impurities capable of functioning as recombination centers.
- (c) Measured radiative coloration dose-dependent, thus permitting laboratory simulation at a proton flux several orders of magnitude higher than solar.

As a result of experimentation carried out during this second year the above premises require certain modification as follows:

- (a) Proton damage occurs in the bulk, probably as a result of $e' - h'$ diffusion from a constant, p^+ -generated pair density in the surface. This bulk damage is the determining factor in radiative coloration and is slow to saturate.
- (b) The roles of impurities as (1) color centers and as (2) recombination centers affecting the kinetics of other intrinsic centers are not identical and must be defined.

(c) Radiative coloration continues to appear dose-dependent only. The following discussion represents an attempt to illustrate and, where possible, conceptually formulate certain relevant optical damage kinetics induced by low energy proton irradiation. Evidence will be presented which illustrate charge carrier diffusion into the bulk followed by trapping at both native (intrinsic, e.g., Schottky) and foreign (extrinsic) defects.

4.1 EVIDENCE FOR CHARGE CARRIER DIFFUSION

In experiment (-71), a period of p^+ -irradiation of a MgO single crystal resulted in decreasing the density of Fe^{2+} from an initial value of $4.1 \times 10^{17}/cm^3$ to a final value of $2.3 \times 10^{17}/cm^3$, both values averaged over a measured bulk thickness ≈ 0.1 cm. On the basis of an incident surface of $1. cm^2$, the bulk crystal volume $\approx 0.1 cm^3$, a volume containing $4.1 \times 10^{16} Fe^{2+}$. These ions are initially uniformly distributed in the bulk. The volume associated with the p^+ -range ($\approx 10^{-6} cm^3$) accounts for only $4.1 \times 10^{11} Fe^{2+}$ initially. Even if all of these Fe^{2+} in the "surface" layer changed valence state during the p^+ -bombardment, such changes could not account for the measured decrease of $1.8 \times 10^{16} Fe^{2+}$ ($= 4.1 \times 10^{16} - 2.3 \times 10^{16}$).

Consistent evidence of this kind, involving net capture or release of an e' or h' by impurities located in the bulk as well as the surface, indicates $e' - h'$ pair diffusion into the bulk. Such diffusion results in the establishment of a significant density of free h' and e' at crystal

depths of the order of one-half or more of the crystal thickness x . In addition, data presented later indicates that such diffusion (as modified by $e' - h'$ recombination and trapping) controls the growth rate of the observed color center bands.

4.2 OPTICAL DAMAGE KINETICS

A single damage model embracing all concurrent and sequential defect processes has proven to be unmanageable. This conclusion rests on the following basis:

- a. A solution of the $e' - h'$ pair diffusion equation with recombination and trapping is very complex.
- b. Complete characterization of native defect structure is almost impossible.
- c. Many optical resonant states are not identified.
- d. Precise effects of many substitutional impurities are not yet understood, e.g. Al^{3+} and Si^{4+} in MgO.

These complexities do not preclude limited analysis of certain observed electronic processes of real importance to the ultimate problem of achieving radiative stability in a white pigment.

4.2.1 Band Gap Considerations

An estimated energy level diagram is presented below (Figure 14) as an aid in following subsequent arguments. Note that only selected trapping and recombination levels are shown. These are established at thermal levels within the band gap based on available data or as inferred from reported qualitative thermal bleaching studies. Known thermal levels are:

$$\begin{aligned}
 V'_{Mg} &\equiv V_1 \text{ center : } 1.1 \text{ eV above valence band}^{13} \\
 (OH - V'_{Mg})^x &\equiv V_{OH} \text{ center : } 0.84 \text{ eV above valence band}^4 \\
 V_O^x &\equiv F \text{ center : } 1.53 \text{ eV below conduction band}^{14} \\
 F^+ &: <0.01 \text{ eV (i.e. unstable above } 20^\circ K)^3
 \end{aligned}$$

Note: See also Professor Kroger's¹⁸ electronic energy level schematic for MgO + Fe + Li based on Schottky disorder.

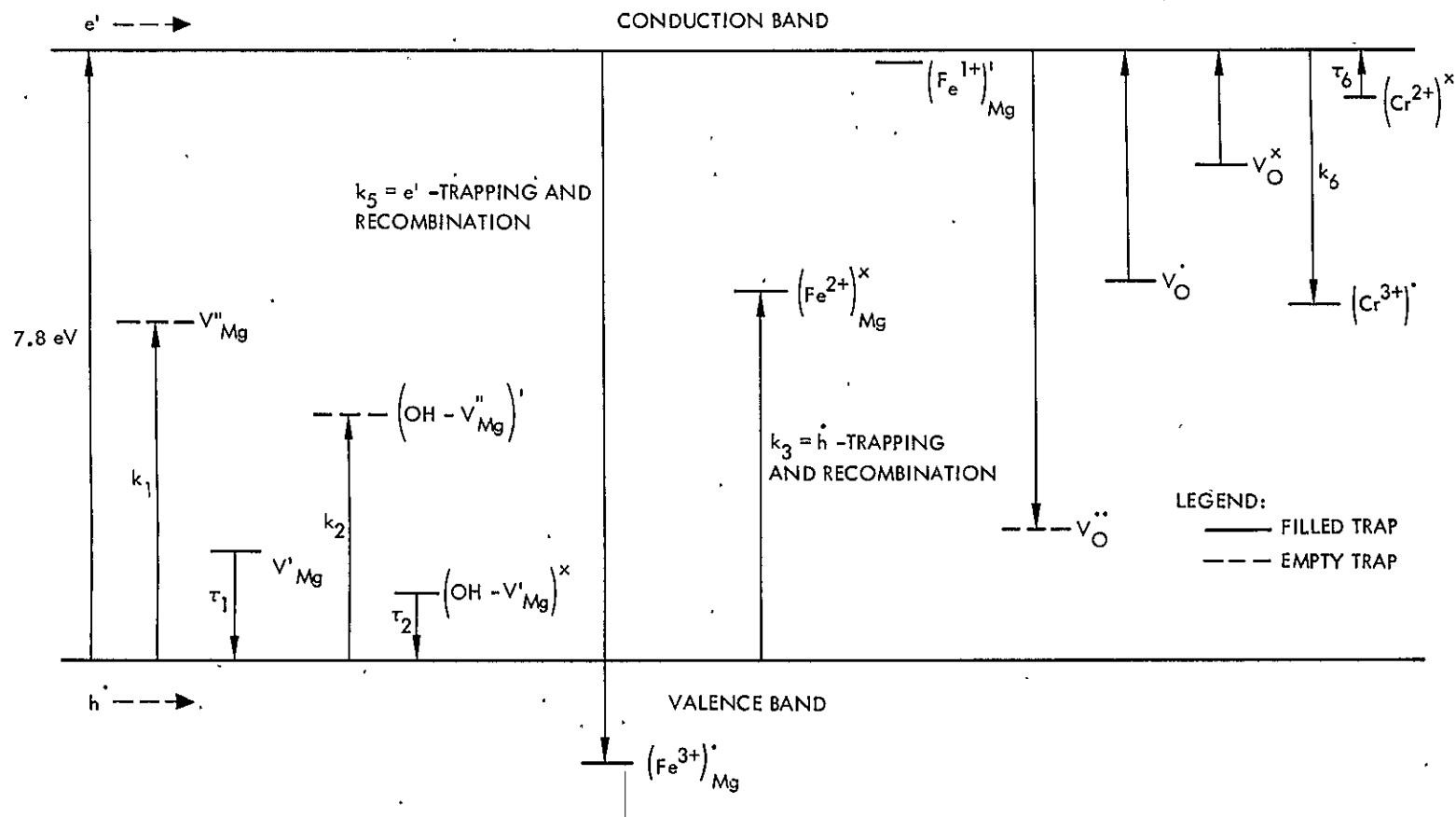


Figure 14. Schematic electron energy level diagram for selected defects in MgO

Hole trapping is designated by an arrow pointing upwards from the valence band, hole release by a reverse direction. Electron trapping is shown by an arrow pointing downwards from the conduction band, electron release by a reverse direction. In addition, the following symbols are used:

- H = total density of isolated V_{Mg}'' , with and without a trapped hole
 H^* = total density of $OH - V_{Mg}''$ pairs, with and without a trapped hole
 p = density of free holes
 p_H = density of holes trapped at $H = [V_{Mg}'] = [V_1 \text{ centers}]$
 p_{H^*} = density of holes trapped at $H^* = [OH - V_{Mg}']$
 $= [V_{OH}] \text{ centers}$,
 k = rate constant for trapping (cm^2/sec) = $\bar{v} \sigma$
 τ = time constant for thermal release from trap, sec
 t = time, sec

4.2.2 Growth Rate of Fe^{3+} Band in the Bulk

Figure 15 illustrates the growth in the density of Fe^{3+} in the bulk with p^+ fluxes of the order of $3. \times 10^{11}$ to $3.4 \times 10^{11} p^+/\text{cm}^2\text{-sec}$. This growth reflects a net conversion of $Fe^{2+} \rightarrow Fe^{3+}$ whose rate at some particular point in the bulk may be expressed in terms of their densities as follows:

$$\frac{d [Fe^{3+}]}{dt} = k_3 p_{(x)} [Fe^{2+}] \quad (1)$$

Estimation of the hole density depth-dependence $p_{(x)}$, as established by $e^- - h^+$ diffusion from a "surface layer", constitutes the problem. This will be attempted parametrically, rather than rigorously, for reasons mentioned earlier.

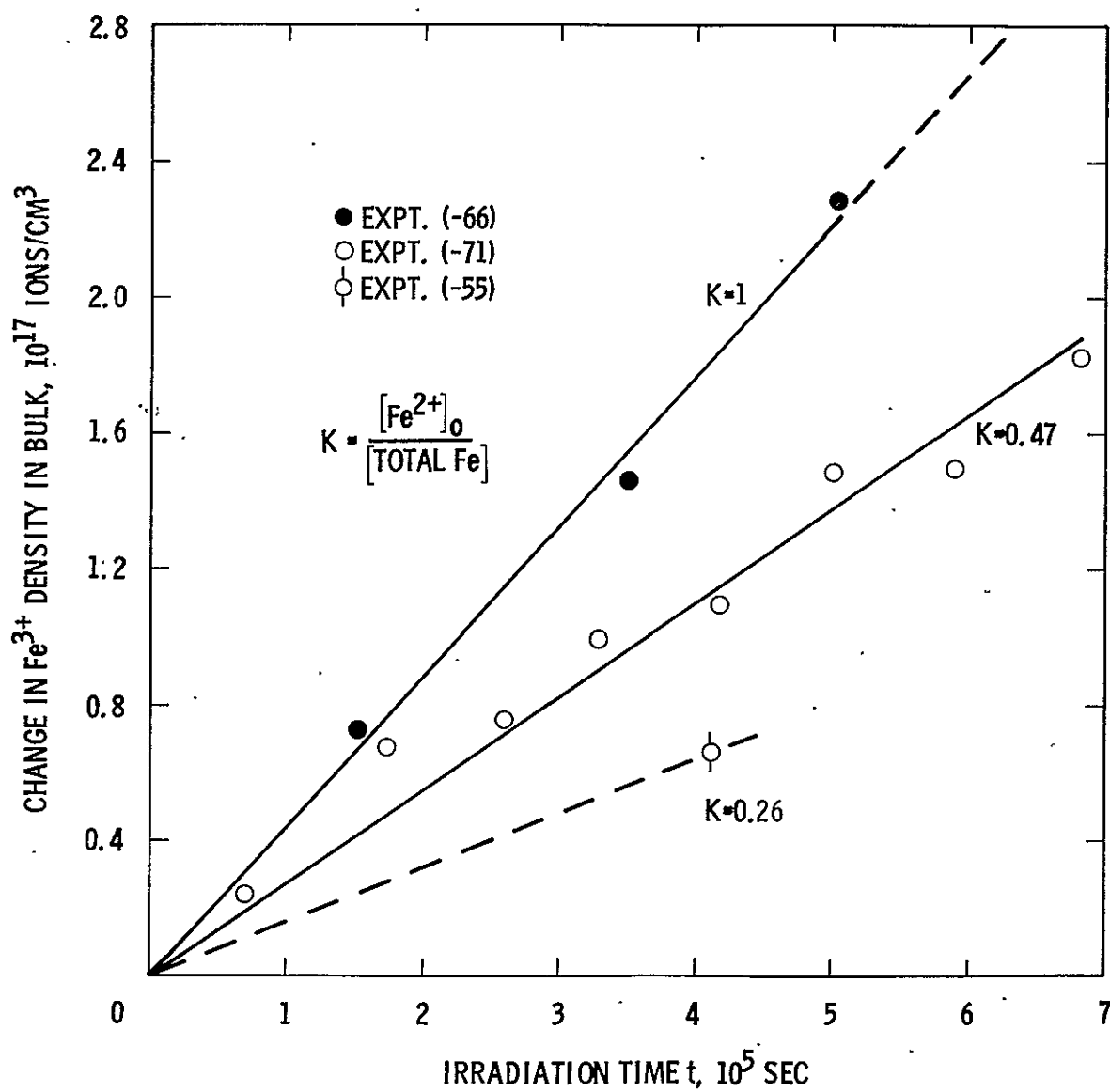


Figure 15. Measured growth of Fe^{3+} density induced in the bulk of various MgO single crystals by 1.0 keV proton irradiation (neutral beam) at a flux of 3.0×10^{11} to 3.4×10^{11} $\text{p}^+/\text{cm-sec}$

If $U(x)$ represents a solution of the $e' - h'$ pair diffusion equation, then $p_{(x)}$ varies as:

$$p_{(x)} = p_s U_{(x)} \quad (2)$$

where:

p_s = hole density in surface layer

Due to the high pair generation rate in the limited surface volume, at some time, short compared to experimental times e.g. 6×10^5 sec, the following occur:

a. In the surface:

(1) Defect densities saturate so that $p_{\text{surface}} (p_s)$ approaches a steady state value

(2) Fe^{2+}/Fe^{3+} equilibration occurs. Thus

$$[Fe^{2+}]_{\text{surface}} \propto [\text{total Fe}]$$

b. A fixed distribution of hole density from the surface layer into the bulk is established, i.e. $U_{(x)} \approx \text{constant}$.

Similar to earlier work we may write an expression for the time-dependence of p in the surface as follows:

$$\begin{aligned} \frac{dp}{dt} = & g - k_3 p_s [Fe^{2+}]_s - k_2 p_s (H^* - p_{H^*}) + p_{H^*}/\tau_2 \\ & - k_1 p_s (H - p_H) + p_H/\tau_1 \end{aligned} \quad (3)$$

where:

g = proton generation rate of $e' - h'$ in the surface
 $\approx 10^{19}$ pairs/cm³ - sec

Note that upon early defect saturation in the surface layer (proton range) : $dp/dt \rightarrow 0$, $p_{H^*} \rightarrow H^*$, and $p_H \rightarrow H$. Based on reported thermal release values at room temperature of $\tau_1 \approx 2.5 \times 10^4$ sec and $\tau_2 \approx 3.5 \times 10^2$ sec and saturation values of $p_{H^*} \approx 3.5 \times 10^{17}/\text{cm}^3$ and $p_H \approx 0.8 \times 10^{17}$, $p_{H^*}/\tau_2 \approx 10^{15}/\text{cm}^3\text{-sec}$ and $p_H/\tau_1 \approx 3 \times 10^{12}/\text{cm}^3\text{-sec}$. Note that these last two values are much

smaller than g . As a consequence, equation (3) approaches the following upon surface saturation:

$$0 \approx g - k_3 p_s [\text{Fe}^{2+}] \quad (4)$$

or

$$p_s \approx \frac{g}{k_3 [\text{Fe}^{2+}]_s} \quad (5)$$

Based on note a. (2) above, equation (5) may be restated as follows:

$$p_s \approx \frac{(\text{constant}) g}{k_3 [\text{total Fe}]}$$

or

$$p_s \propto \frac{1}{[\text{total Fe}]} \quad (6)$$

From equation (2) and the assumption $U_{(x)} = \text{constant}$, we estimate that:

$$p_{(x)} \propto \frac{1}{[\text{total Fe}]} \quad (7)$$

Rewriting equation (1) in terms of (7) yields:

$$\frac{d[\text{Fe}^{3+}]}{dt} = k_3 C' \frac{[\text{Fe}^{2+}]}{[\text{total Fe}]} \quad (8)$$

and we observe that the growth rate of Fe^{3+} in the bulk (see Table 5) depends on the ratio of the densities of Fe^{2+} and total Fe. Since there is evidence (Figure 16) that in our experiments we are considerably removed from saturation in the bulk, we might compare experimental rising kinetics on the basis of initial Fe^{2+} densities in the bulk, i. e. $[\text{Fe}^{2+}]_0$.

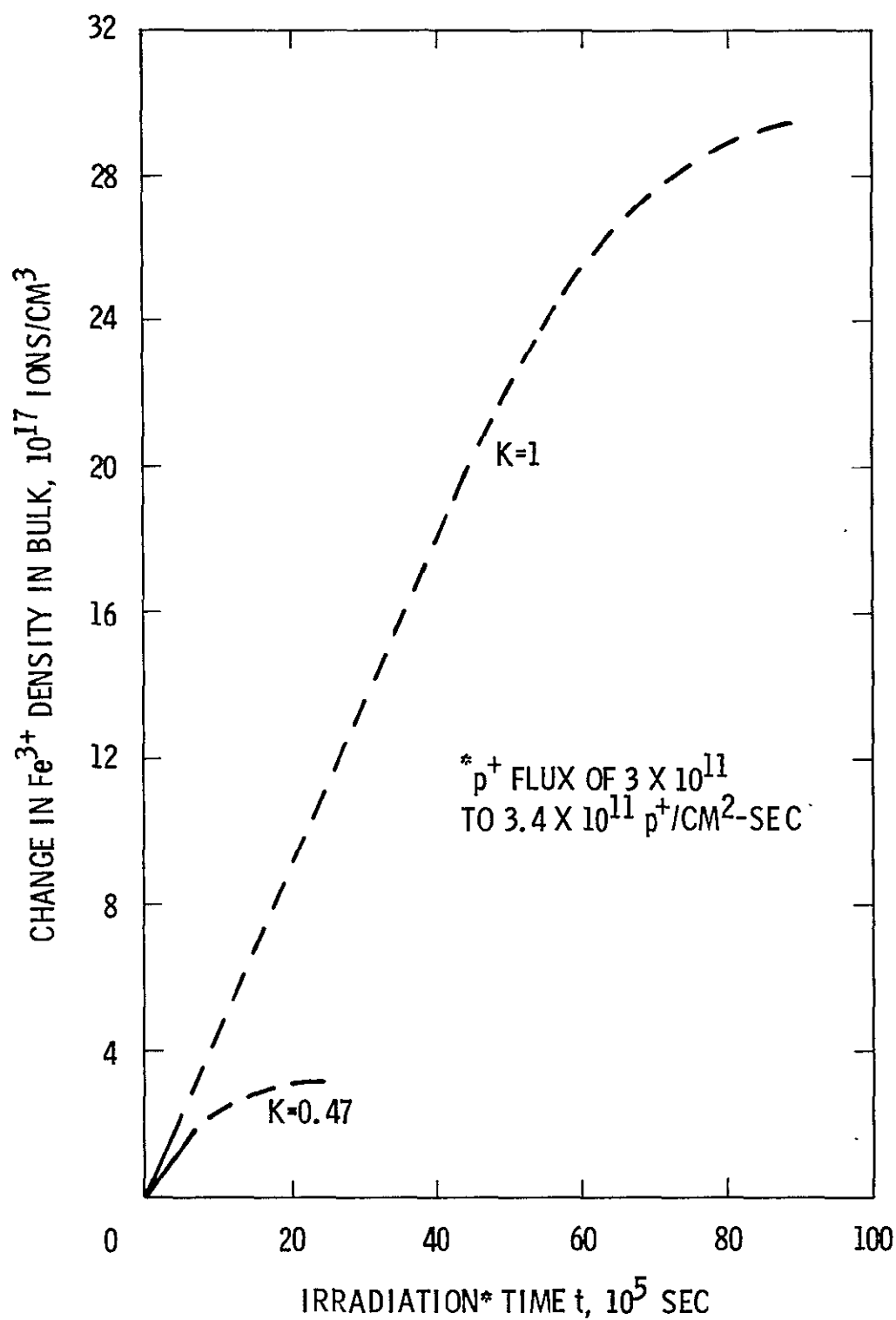


Figure 16. Estimated p^+ -induced growth to saturation of Fe^{3+} in the bulk of two MgO single crystals

Table 5. Estimated Fe^{3+} Growth Rate Dependence in the Bulk

Experiment No.	$[\text{Fe}^{2+}]_o$, $10^{17}/\text{cm}^3$	$[\text{tot. Fe}]$, $10^{17}/\text{cm}^3$	$\frac{[\text{Fe}^{2+}]_o}{[\text{tot. Fe}]}$
(-66)	42.	42.	1.
(-71)	4.1	8.7	0.47
(-55)	0.7	2.7	0.26

Comparison of Figure 15 with the ratios in column four above indicates reasonable agreement between analysis and experiment as shown in Table 6. Thus we conclude that the rising kinetics for Fe^{3+} approach linearity and are dependent on the ratio $[\text{Fe}^{2+}] / [\text{total Fe}]$.

Table 6. Comparison Between Computed and Experimental Normalized Growth Rates for Fe^{3+} in the Bulk

Experiment No.	$d[\text{Fe}^{3+}]/dt$ (normalized to expt. -55 values)	
	Computed	Experiment
(-66)	3.8	2.8
(-71)	1.8	1.7
(-55)	1.	1.

4.2.3 Growth Rate of V_1 Center

In the bulk of the crystal, the following expression for $p(x, t)$ holds true:

$$\frac{\partial p(x, t)}{\partial t} = -D \frac{\partial^2 p}{\partial x^2} - k_3 p [\text{Fe}^{2+}] - k_2 p (H^* - p_{H^*}) + p_{H^*} / \tau_2$$

$$= k_1 p (H - p_H) + p_H / \tau_1 \quad (9)$$

where: $p = p(\vec{x})$

Previous assumptions (Section 4.2.2) of early surface saturation and early establishment of a constant p-distribution ranging from the surface layer into the bulk are retained. Thus as in equation (7),

$p_{(x)} \propto [\text{total Fe}]^{-1}$. Note that the diffusion term, first term in equation (9), is positive since $\partial^2 p / \partial x^2$ (assumed constant) is always negative. The time-dependence of p_H at a given x may be written as an ordinary differential as follows:

$$dp_H/dt = k_1 p_{(x)} (H - p_H) \quad (10)$$

where the back reaction, or thermal release, is neglected for rising kinetics. During the rising portion of the kinetics, except near the surface layer, it is likely that $p_H \ll H$ and similarly $p_{H^*} \ll H^*$. Therefore equation (10) may be approximated by:

$$dp_H/dt \approx k_1 p_{(x)} H \quad (11)$$

Substituting $p_{(x)}$ from equation (7) in equation (10) yields:

$$dp_H/dt \propto \frac{1}{[\text{total Fe}]} \cdot H \quad (12)$$

It is important to note that H is crystal-dependent and is not influenced by irradiation. Such dependency is not directly measurable. Hence an alternate evaluation of H will be sought in γ-radiation (in which case the dose is delivered to the crystal bulk) carried to V_1 and V_{OH} center saturation. Time-dependent expressions for p, p_H , and p_{H^*} thus uniformly distributed in the bulk at saturation are as follows:

$$\begin{aligned} dp/dt = 0 = & g - k_3 p [Fe^{2+}] - k_2 p [H^* - p_{H^*}] + p_{H^*}/\tau_2 \\ & - k_1 p [H - p_H] + p_H/\tau_1 \end{aligned} \quad (13)$$

$$dp_H/dt = k_1 p [H - p_H] - p_H/\tau_1 = 0 \quad (14)$$

$$dp_{H^*}/dt = k_2 p [H^* - p_{H^*}] - p_{H^*}/\tau_2 = 0 \quad (15)$$

Substitution of equations (14) and (15) into (13) yields:

$$p = \frac{g}{k_3 [Fe^{2+}]_n} \quad (16)$$

where:

$g = e' - h'$ pair generation rate

subscript n indicates density at saturation

Substitution of (16) into (14) followed by rearrangement yields:

$$H = \frac{k_3 [Fe^{2+}]_n}{k_1 g} \left\{ \frac{k_1 g}{k_3 [Fe^{2+}]_n} + \frac{1}{\tau_1} \right\} (p_H)_n \quad (17)$$

Exact evaluation of equation (17) is prevented by a lack of values for k_3 and k_1 . In lieu of this, it may be expressed as the proportionality:

$$H \propto [Fe^{2+}]_n (p_H)_n \left\{ \frac{k_1 g}{k_3 [Fe^{2+}]_n} + \frac{1}{\tau_1} \right\} \quad (18)$$

Combining equations (12) and (18) yields a single scaling expression for comparing experiments as follows:

$$dp_H/dt \propto \frac{1}{[total Fe]} [Fe^{2+}]_n (p_H)_n \left\{ \frac{k_1 g}{k_3 [Fe^{2+}]_n} + \frac{1}{\tau_1} \right\} \quad (19)$$

On the basis of a γ -dose (absorbed) of approximately 1 Mrad/hr and an ionization requirement of ~ 20 eV per $e^- - h^+$ pair, pair generation g is estimated as follows:

$$g = \frac{10^6 \text{ rad (100 erg/g)}(6.2 \times 10^{11} \text{ eV/erg})(3.58 \text{ g/cm}^3)}{\text{hr (3600 sec/hr)}(20 \text{ eV/pair})}$$

$$g = 3.1 \times 10^{15} \text{ pairs/cm}^3\text{-sec} \quad (20)$$

Recall from earlier discussion that $\tau_1 \approx 2.5 \times 10^4$ sec.

If one further assumes a value for $k_3/k_1 \approx 250$, the rising kinetics shown in Figure 17 may be explained. Note that in the first year's effort¹², this ratio of k_3/k_1 was estimated as 1000. A value of 250 seems quite reasonable.

Comparison of the V_1 center rising kinetics (dp_H/dt) for experiments (-71) and (-66) are based on the following measured values:

<u>Experiment No.</u>	10^{17} Ions or Defects/cm ³		
	<u>[total Fe]</u>	<u>[Fe²⁺]_n</u>	<u>[V₁]_n \equiv (p_H)_n</u>
-66	42.	12.	1.
-71	8.7	1.(est.)	0.79

Table 7 which follows may then be constructed according to the scaling directed by equation (19).

The result computed in column seven is that the product of scaling factors for experiments (-66) and (-71) are the same. This predicts that their rising kinetics for the V_1 center coincide, a prediction verified in Figure 17. The early induction period indicated is not yet understood. No saturation data for γ -irradiation of experiment

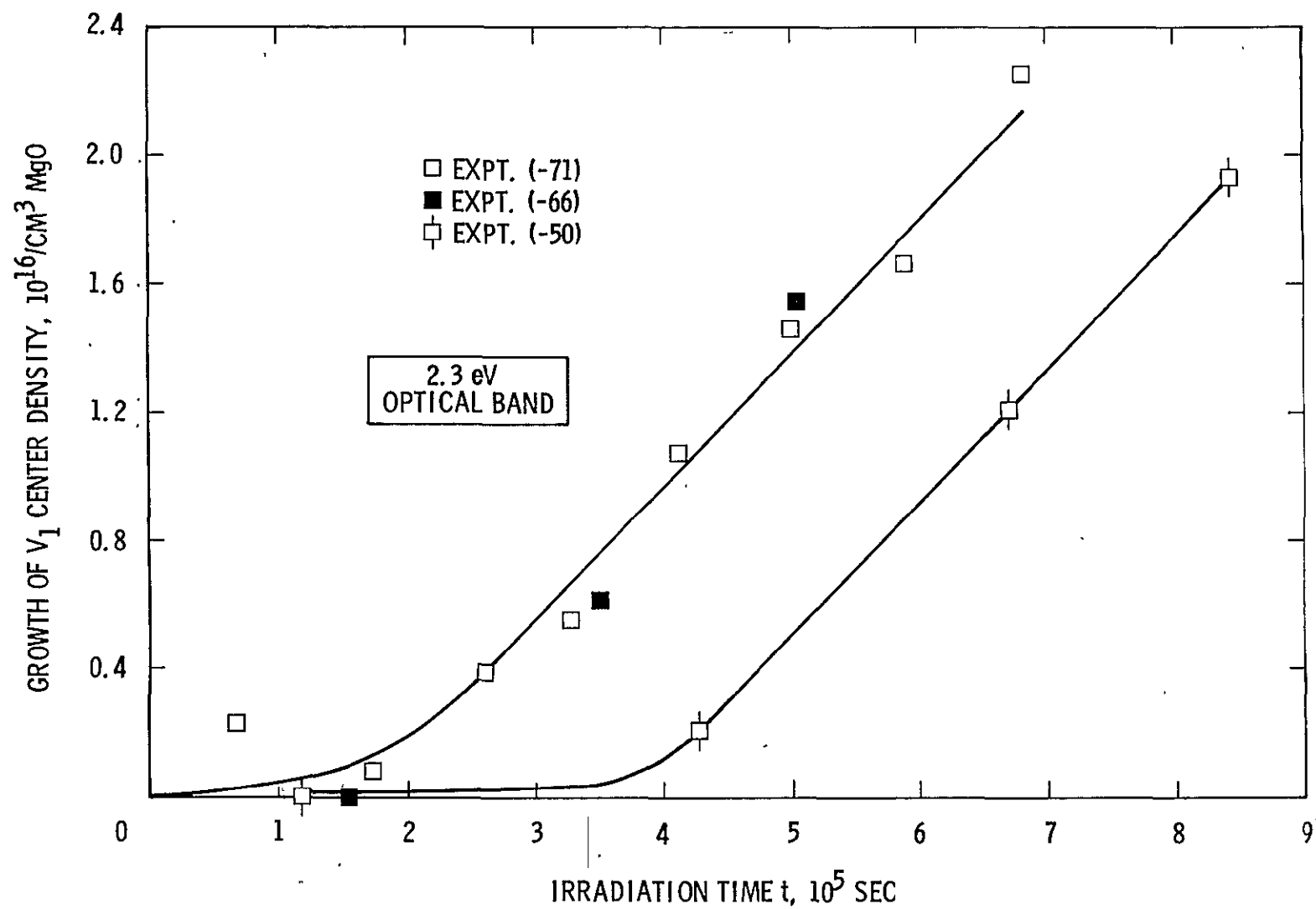


Figure 17. Measured growth of V_1 center induced in various MgO single crystals by 1.0 keV proton irradiation (neutral beam) at a flux of 3.0×10^{11} to $3.4 \times 10^{11} \text{ p}^+/\text{cm}^2\text{-sec}$

Table 7. Scaling Factors for Comparing the Growth Rate of V_1 Center ($dV_1/dt = dp_H/dt$) in Experiments (-66) and (-71)

Experiment No.	$\frac{1}{[\text{total Fe}]}$	Factors Which Reveal H				$dp_H/dt \propto$ (Product of Columns 2 and 6)
		$[\text{Fe}^{2+}]_n$	Curly Bracket in Equation (18)	$(P_H)_n$	$H \propto$ Product of Columns 3, 4, & 5	
-66	0.238	12.	0.061	1.0	0.731	0.18
-71	1.15	1.	0.199	0.79	0.157	0.18

(-50) was available for correlation. It is interesting to note however that the early V_1 center generation rate observed in this case appears identical with those for (-66) and (-71), after a longer period of delay.

4.2.4 Kinetics of Miscellaneous Centers

The optical band peaking at 3.6 eV is thought to represent an intrinsic defect containing a trapped electron. Except for slightly different induction periods, early growth rates for this band appear crystal-independent (see Figure 18). Pending further identification of this center, no further correlation was attempted.

4.2.5 Effect of Dose Rate on Generation Kinetics

As discussed earlier, this work has involved exposure to proton dose rates of the order of $1000 \times$ the solar wind proton flux. Time integrated fluences equivalent to an order of 30 years exposure in space were delivered. It is thus relevant to ask whether the optical damage would be equivalent between space and the accelerated laboratory experiments.



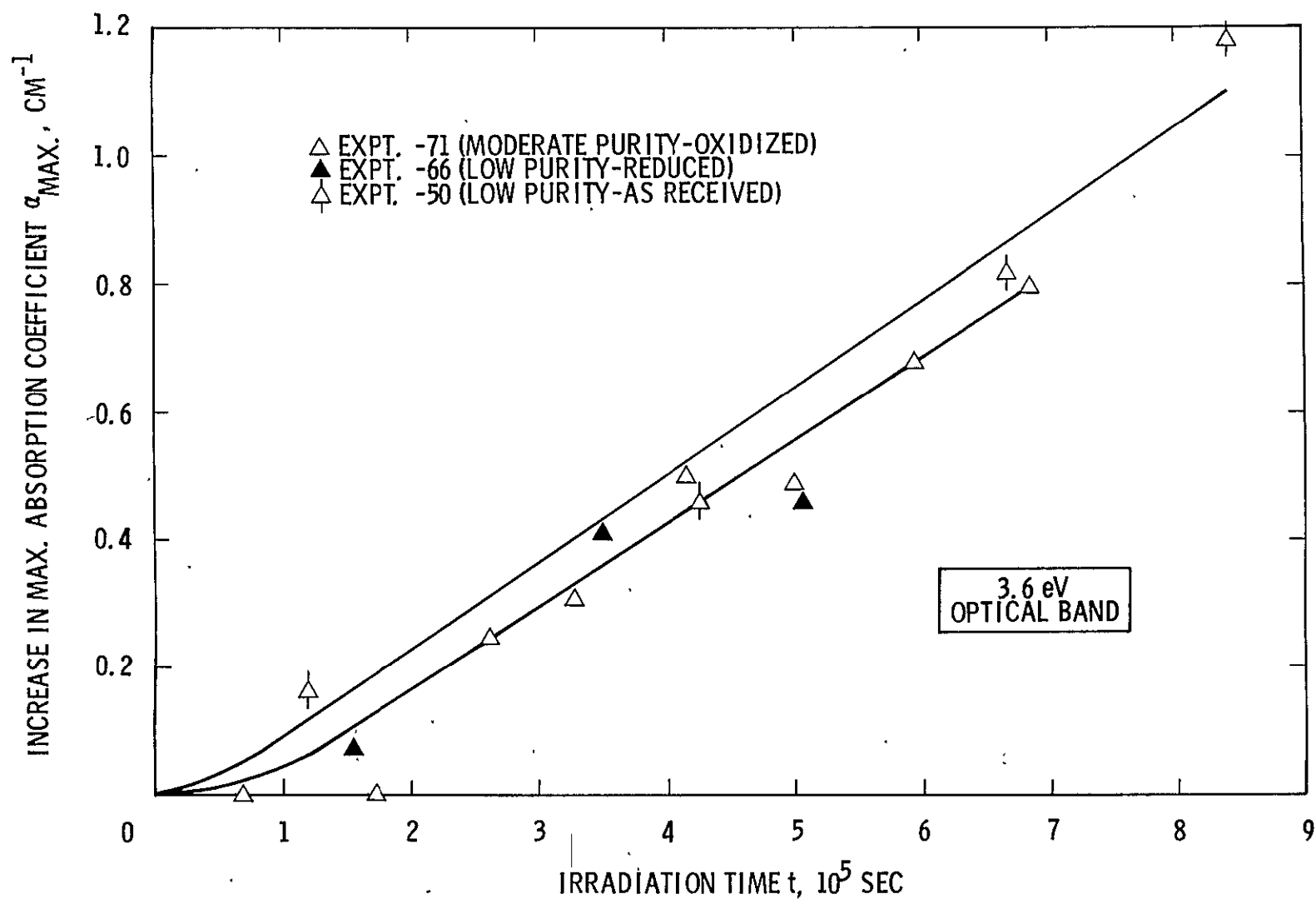


Figure 18. Measured growth of 3.6 eV band in various MgO single crystals by 1.0 keV proton irradiation (neutral beam) at a flux of 3.0×10^{11} to 3.4×10^{11} p^+ /cm²-sec

The argument will be related to the dependence of hole processes in the bulk, although a similar argument for electron processes could be made. The equation for hole processes in the bulk is given again:

$$\begin{aligned} \frac{\partial p(x, t)}{\partial t} = & -D \frac{\partial^2 p(x, t)}{\partial x^2} - k_3 p [Fe^{2+}] - k_2 p (H^* - p_{H^*}) - k_1 p (H - p_H) \\ & + \frac{p_{H^*}}{\tau_2} + \frac{p_H}{\tau_1} \end{aligned} \quad (9)$$

In order to demonstrate strict dose dependence we must show that each term above is directly proportional to the hole generation rate g . Such demonstration permits g to be factored out as a simple time scale factor.

In accord with earlier argument, after some short time period the distribution of free holes is given by:

$$p(x) = p_s U(x) \quad (2)$$

where:

$$U(x) = \text{solution of diffusion equation}$$

also

$$\frac{\partial^2 p}{\partial x^2} = p_s \frac{\partial^2 U}{\partial x^2} \quad (21)$$

For a given value of [total Fe], note from equation (6) that: $p_s \propto g$. Therefore from equations (2) and (21) above we see that:

$$\frac{\partial^2 p}{\partial x^2} \propto g ; p(x) \propto g$$

Thus the first four terms in equation (9) above are shown to be proportional to g . When well below saturation, the thermal release terms (p_H^*/τ_2 , p_H/τ_1) are of lesser importance and may be omitted. Since g is proportional to the proton dose rate g_{p+} , the factor g_{p+} is common to the four remaining terms in equation (9) and may be transposed as a time scale factor thus:

$$\partial p_{(x,t)} / \partial (t \cdot g_{p+}).$$

We therefore conclude that these hole processes are independent of the dose rate g_p . Laboratory acceleration is thus valid in terms of space simulation.

5.0 SUMMARY

This work is associated with the development of improved thermal control coatings for space application. The effort and the conclusions derived therefrom may be summarized as follows:

- a. MgO (both single crystals and polycrystalline material) was selected as a typical dielectric solid transparent to solar (photon) radiation. Numerous specimens were exposed to a neutral, 1.0 keV proton beam in vacuum at a dose rate of 3.0×10^{11} to 3.4×10^{11} $p^+/\text{cm}^2\text{-sec}$ (i.e. an order of 1000 \times the solar wind flux). Changes in optical and EPR spectra were measured in situ during exposure as a means of identifying proton-generated defects (important to radiative coloration) and determining their growth kinetics.
- b. Material emphasis was placed on single crystals because of greater ease in the control of and identification of defect structure compared to powders. Controlled physical processing (thermal) and chemical processing (e.g. oxidation, reduction, iron-doping) of specimens was performed as an integral part of the experimentation.
- c. Resolution of proton-induced optical and EPR spectral displays has been carried out so as to identify important individual defect species and their densities.
- d. Measured changes in impurity defects establish the dominant coloration mechanism as consisting of $e^+ - h^+$ pair diffusion into the crystal bulk from a surface layer (defined by the projected proton range) followed by recombination and trapping in the bulk. This conclusion is in contrast to the first year's theoretical effort wherein damage within the proton range was believed to determine radiative coloration. This diffusion-dependence greatly increases the influence of initial defect structure on the resultant optical damage.

- e. Defect rising kinetics, i.e. well below saturation, are indicated to be dose-dependent. Thus laboratory simulation employing accelerated proton dose rates (relative to space) remain relevant to the work.
- f. Even on an idealized basis, a generalized model describing defect kinetics has not proven feasible. This results from:
 - 1. Lack of definition of many participating defect species.
 - 2. Difficulties in resolution and identification of defects.
 - 3. Complex solution to diffusion equation.
- g. Modeling by resort to scaling factors has proven both feasible and instructive. This has been used to correlate growth rate data for typical foreign defects (e.g. Fe^{3+}) and native defects (e.g. V_1 center) among various experiments.
- h. Comparison of proton-induced spectral absorption in MgO reveals a strong dependence on initial purity (selective) and native defect structure. In this regard, the radiative stability of a processed, high purity crystal was established by the small change, $(\alpha_S)_{\text{initial}} \approx 0.03$ to $(\alpha_S)_{\text{final}} \approx 0.031$, induced by a $2.3 \times 10^{17} \text{ p}^+/\text{cm}^2$ fluence of 1.0 keV protons.

6.0 REFERENCES

1. King, H. J., and Zuccaro, D.E., "Solar Wind Simulation Techniques," NASA CR-73443, pp 61-65 (1970).
2. Chen, Y., and Sibley, W. A., "Study of Ionization-Induced Radiation Damage in MgO," Phys. Rev. 154, 842-50 (1967).
3. Kolopus, J. L., Private Communication
4. Henderson, B., and Wertz, J. E., "Defects in Alkaline Earth Oxides," Advances in Physics 17, 791-4 (1968).
5. Wertz, J. E., Orton, J. W., and Auzins, P., "Spin Resonance of Point Defects in Magnesium Oxide," J. Appl. Phys. 33 (Supplement), 322 (1962).
6. Adam, D. B., and Brindley, G. W., "Cation Solutions in Crystalline MgO of the Type $Mg_{1-x}(R^+, R^{n+})_xO$," Materials Sci. and Engr. 3 (5), 252-4 (1969).
7. Henderson, B., King, R. D., and Stoneham, A. M., "The Temperature Dependence of the F Band in Magnesium Oxide," J. Phys. C (Ser. 2) 1, 586-9 (1968).
8. Hansler, R. L., and Segelken, W. G., "Correlation of Thermoluminescence in MgO and Valence Changes of Iron and Chromium Impurities Detected by EPR," J. Phys. Chem. Solids 13, 130 (1960).
9. Blair, P. M., Jr., "In-Situ Evaluation of Several Thermal Control Coatings," Hughes Aircraft Company Report No. 67-226, pp 7-8 (1967).
10. Haxby, B. V., "A Study of Color Centers in Magnesium Oxide," Ph.D. Thesis, University of Minnesota, pp 24-28 (1957).
11. Glass, A. M., and Searle, T. M., "Reactions Between Vacancies and Impurities in Magnesium Oxide II. Mn^{4+} - Ion and OH^- - Ion Impurities," J. Chem. Phys. 46, 2098 (1967).
12. Levin, H., Honnold, V. R., and Berggren, C. C., "Study of Color Center Formation in White Powder Compounds," NASA CR 73337, pp 30, 41 (1969).
13. Searle, T. M., and Glass, A. M., "The Thermal Decay of the V_1 Center in Magnesium Oxide," J. Phys. Chem. Solids 29, 609-14 (1968).

14. Kroes, Roger L., "Color Centers in Magnesium Oxide," Ph.D. Thesis, University of Missouri, p. 59 (1968).
15. Schall, P., "Effect of Atomic Displacements on Color Center Production in MgO," J. Phys. Chem. Solids 28 1211-23 (1967).
16. Clark, F. P., "Irradiation Damage in Single Crystals of Magnesium Oxide," Trans. Far. Soc. 2 (Ser. 8), 607-27 (1957).
17. Kats, A., "Hydrogen in Alpha-Quartz," Philips Res. Rept. 17, 223-228 (1962)
18. Kröger, F. A., "Point Defects in Compounds and Their Role in Diffusion," Sintering and Related Phenomena, Kuczynski, G. C., Hooton, N. A., and Gibbon, C. F., Editors, Gordon and Breach Science Publishers, New York, p 40 (1967).

APPENDIX A

ANALYSIS OF OPTICAL MEASUREMENTS

1.0 SINGLE CRYSTAL STUDIES

Meaningful interpretation of proton-induced optical absorption or reflection changes (as indicated say in Figure 7) require resolution of the measured values into discrete component spectra, each indicative of a particular defect species. Further required is the establishment of a relation between measured, total spectral reflectance ($R_\lambda \equiv R$) and changes in defect densities, e. g. by means of derived values of the total spectral absorption constant ($\alpha_\lambda \equiv \alpha$).

1.1 RELATION BETWEEN $\Delta\alpha$ AND R

Note that α sums all individual bands thus:

$$\alpha = \sum [\alpha_1 + \alpha_2 + \alpha_3 \text{ etc.}] = [\sigma_1 N_1 + \sigma_2 N_2 + \text{etc.}] \quad (\text{A-1})$$

The Fresnel reflection r at the air-surface interface is defined in terms of the index of refraction n' of the crystal material:
 $r = [(n' - 1)/(n' + 1)]^2$. Optical ray schematics (Figure A-1) are useful for visualizing various terms in the relationship being sought.

For wavelengths $0.21 < \lambda < 2.5 \mu$, $r < 0.10$. As a consequence, terms containing r^2 are quite small and may be omitted. Terms in r and the large R_m term are as follows:

- Basis: (a) α is associated with total crystal thickness x .
 (b) Reflection at mirror second surface = R_m . First surface mirror reflection (Suprasil) is ignored.
 (c) Secondary back reflection resulting from multiple internal crystal reflection is accumulated as in Figure (b) above: $\Sigma r_2 = r_2 + r_2' + r_2'' \text{ etc.}$
 (d) The attenuation factor $e^{-\sigma x}$ represents the internal absorption in one pass normally through x .

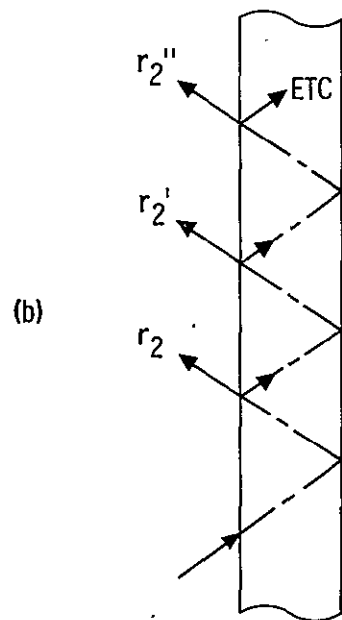
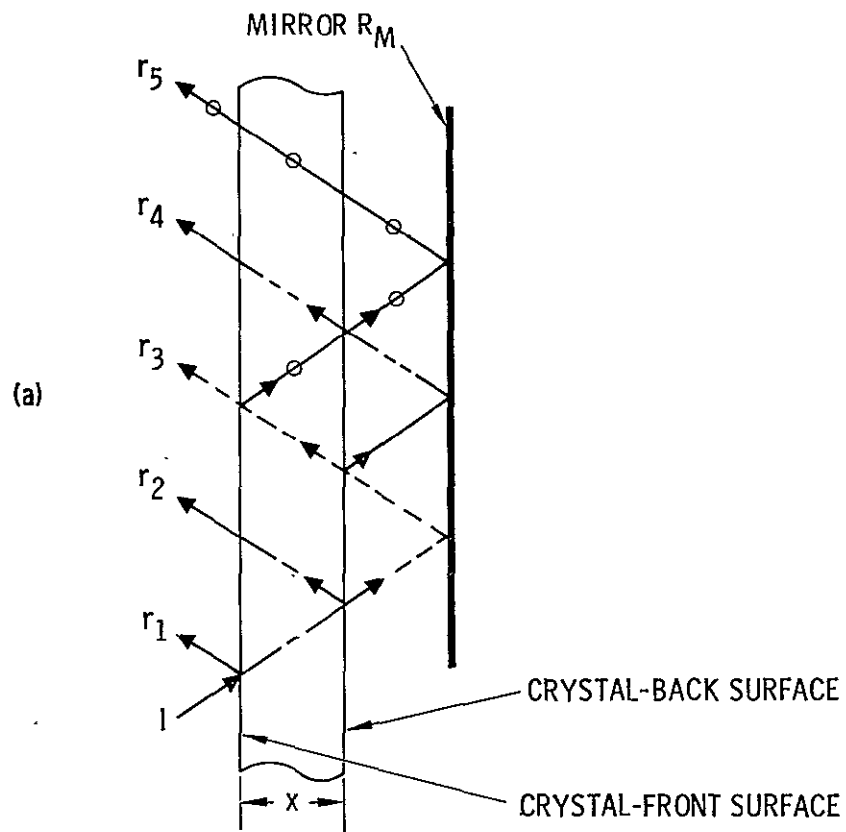


Figure A1. Optical reflectance schematic

$$r_1 = r \quad (A2)$$

$$\begin{aligned} \sum r_2 &= r(1-r)^2 e^{-2\alpha x} + \left[r(1-r) e^{-2\alpha x} \right] r^2 (1-r) e^{-2\alpha x} \\ &+ \left\{ \left[r(1-r) e^{-2\alpha x} \right] r^2 e^{-2\alpha x} \right\} r^2 (1-r) e^{-2\alpha x} \dots \\ &= r(1-r)^2 e^{-2\alpha x} \left[1 + r^2 e^{-2\alpha x} + r^4 e^{-4\alpha x} \dots \right] \end{aligned} \quad (A3)$$

Similarly:

$$\sum r_3 = R_m (1-r)^4 e^{-2\alpha x} \left[1 + r^2 e^{-2\alpha x} + r^4 e^{-4\alpha x} \dots \right] \quad (A4)$$

$$\sum r_4 = r(1-r)^4 R_m^2 e^{-2\alpha x} \left[1 + r^2 e^{-2\alpha x} + r^4 e^{-4\alpha x} \dots \right] \quad (A5)$$

$$\sum r_5 = r(1-r)^6 R_m^2 e^{-4\alpha x} \left[1 + r^2 e^{-2\alpha x} + r^4 e^{-4\alpha x} \dots \right] \quad (A-6)$$

The bracket factor is a geometric series with common ratio $r^2 e^{-2\alpha x}$ and first term = 1. The sum of such a series is: $\left[1 - r^2 e^{-2\alpha x} \right]^{-1}$. Summing (A2) through (A5) and substituting the series sum for the bracket factor yields:

$$\begin{aligned} R = \sum r_n &\approx r + \frac{e^{-2\alpha x}}{1 - r^2 e^{-2\alpha x}} \left[r(1-r)^2 + R_m (1-r)^4 \right. \\ &\left. + r(1-r)^4 R_m^2 \right] + \frac{r(1-r)^6 R_m^2 e^{-4\alpha x}}{1 - r^2 e^{-2\alpha x}} \end{aligned} \quad (A7)$$

For reasonable values of α , the third term in (A7) becomes small and can be dropped. Also the expression $[1-r^2 e^{-2\alpha x}]^{-1}$ approaches a value of one.

$$\therefore R \approx r + \left[r(1-r)^2 + R_m(1-r)^4(1+rR_m) \right] e^{-2\alpha x} \quad (A8)$$

Designating R_o as the measured spectral reflectance before irradiation and R_t as that corresponding to some period of irradiation, equation (A8) may be written:

$$R_o - r \approx [\text{bracket factor}] e^{-2\alpha_o x} \quad (A9)$$

$$R_t - r \approx [\text{bracket factor}] e^{-2\alpha_t x} \quad (A10)$$

Dividing (A9) by (A10) yields:

$$(R_o - r)/(R_t - r) \approx e^{2(\alpha_t - \alpha_o)x} = e^{2\Delta\alpha x} \quad (A11)$$

This may be simplified to yield:

$$\Delta\alpha \approx \frac{1}{2x} \ln \left[\frac{R_o - r}{R_t - r} \right] \quad (A12)$$

From equation (A12) it can be seen that errors become significant at low reflectance values (when $R \rightarrow r$) and at high reflectance values (when $R_t \rightarrow R_o$). These represent the minority of cases. In the remainder errors of the order of 5 percent are considered typical.

Examination of measured reflectance values of unirradiated high purity materials in a spectral region where $\alpha \rightarrow 0$ (e.g. $\lambda = 680$ nm), indicated slightly low values (3 to 7 percent) as a result of losses in striations, between crystal joints in the mosaic array etc. Adding back these losses (on the assumption that they are wavelength-independent) and normalizing to R_m with values calculated by (A7) when $\alpha = 0$) yields the estimated values of spectral absorption α_λ given in Figures 8 and 11.

1.2 GAUSSIAN ANALYSIS

This analysis is based on the following set of spectral band parameters at 20°C:

<u>Band No.</u>	<u>Designation</u>	<u>Location of Band Peak, in eV</u>	<u>Band Width at Half-Max., W in eV</u>	<u>Reference No.</u>
1	Composite (unknown composition)	5.9 (est.)	0.96 (est.)	--
2	F^+	4.91	0.65	7
3	C_r^{2+}	4.85	0.60 (est.)	15
4	F_e^{3+}	4.25	0.99	4
5	Unknown	3.6	0.60 (est.)	4
6	Unknown	3.1	0.44 (est.)	16
7	Unknown	2.7	0.52 (est.)	16
8	V_1	2.3	1.07	2
9	Unknown	2.2 (2.15)	0.50 (est.)	4

A major problem, as noted in the main text earlier, is the lack of definition in the near UV at $(h\nu) > \sim 5$ eV. Several bands are believed to be in this region between 5 eV and the band edge of ~ 8 eV, including

one known to be associated with an Fe^{3+} transition. Additionally, the F^+ and F bands are almost superimposed in the vicinity of 5.eV and overlap the adjacent Cr^{2+} band. As a consequence, spectral resolution in the region $(h\nu) > 4.8$ eV proved difficult and the results poor. Additionally, assumption of a Gaussian distribution may not be valid for certain of the observed bands. Estimated values indicated above were obtained by hand fit of experimental data.

Let $y = \Delta\alpha$ as obtained from (A12). Minimize the function, $\phi = \sum (y - \hat{y})^2$ where y = measured value and \hat{y} = the calculated value. Note that \hat{y} can be expressed linearly in terms of each of the above nine components as follows:

$$\hat{y} = A_1 X_1 + A_2 X_2 \text{ --- etc.} \quad (\text{A13})$$

where:

$$X = \frac{1}{\sqrt{2\pi}\sigma} \exp \left[-\frac{(E - E_o)^2}{2\sigma^2} \right] \quad (\text{A14})$$

σ = standard deviation

E = variable photon energy, eV

E_o = $h\nu$ at component peak, eV

Since the front factor in (A14) can be included in the coefficients A_1 , A_2 etc. in (A13), we may write:

$$X = \exp \left[-\frac{(E - E_o)^2}{2\sigma^2} \right] \quad (\text{A15})$$

From the definition of a Gaussian distribution it can be shown that:

$$\sigma = \frac{w}{\sqrt{2 \ln 2}} \quad (\text{A16})$$

where:

$$w = (E - E_0) \text{ at half max.}$$

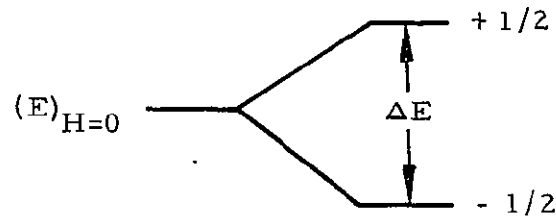
$$= W/2$$

Computer solution of (A13) in terms of a least squares fit of the measured data was obtained.

APPENDIX B

ANALYSIS OF EPR MEASUREMENTS*

The physical basis for electron paramagnetic resonance depends on the spin magnetic moment or the orbital magnetic moment or both of an unpaired electron about the nucleus of a paramagnetic species. In the presence of an external d-c magnetic field of strength H (in gauss), two quantum states will be associated with the combined magnetic moment, μ , of the unpaired electron. When electron spin moment is parallel to the field the energy is $E = \mu H$; when antiparallel, $E = -\mu H$. These two allowed states are thus separated by an energy difference $\Delta E = \mu H - (-\mu H) = 2\mu H$. The value 2μ may be replaced by the product $g\beta$, where g is a dimensionless variable called the spectroscopic splitting factor (and equals the ratio of the total magnetic moment to the spin magnetic moment) and β is a constant ($=9.27 \times 10^{-21}$ erg/gauss) designated the Bohr magneton. The factor g is characteristic of the atomic environment of the electron and for a completely free electron $g = 2.0023$. Larger values typically indicate trapped holes and smaller values trapped electrons. This splitting of electron energy levels by a magnetic field H may be shown schematically as follows:



where

$$\Delta E = g\beta H \quad (B1)$$

*Abstracted from: Blair, P. M. Jr., Levin, H., Honnold, V. R., and Peffley, W. M., "Study of the Combined Effects of Space Environmental Parameters on Space Vehicle Material," George C. Marshall Space Flight Center NAS 8-21087 (Dec. 1969).

In order to effect a transition from lower to upper quantum energy level, electromagnetic radiation can only be absorbed at a frequency ν given by:

$$\Delta E = h\nu \quad (B2)$$

where: h = Planck's constant = 6.63×10^{-27} erg-sec

From the above one obtains the following:

$$h\nu = g\beta H$$

and

$$\nu = (g\beta/h)H \quad (B3)$$

For a free electron, the resonant or absorption frequency is:

$$\nu = \frac{(2.0023)9.27 \times 10^{-21} H}{6.63 \times 10^{-27}} = 2.80H \quad (B4)$$

where: ν is in MHz and H is in gauss

Thus by use of a d-c magnetic field of 3400 gauss, one may obtain energy absorption at a convenient microwave frequency of the order of 9500 MHz.

The conventional procedure is to tune the microwave cavity containing the specimen to some precise frequency near 9500 MHz and then vary (scan) the magnetic field until absorption of the microwave energy is noted. The resonant signal thus obtained is displayed on a strip chart recorder, generally in the form of the derivative of the absorption line. This line can be studied in a way that is similar to methods used in other more familiar resonant phenomena.

Briefly, the following types of information on a radiation induced electron center can be deduced from a study of its resonance signal. If the resonance line is fairly narrow, the density of the centers can be estimated by a comparison of the intensity of the signal with that from a standard, usually an organic free radical. In a study of the kinetics of the formation and decay of a center formed by radiation, the change of the amplitude of the signal with time will give a direct indication of the dependence of the density with time. In some cases, the electron in a metastable state will interact with the nuclear spins of surrounding atoms. This interaction ("hyperfine interaction") can cause a splitting of the observed resonance line. When this splitting is resolved, the number of hyperfine lines gives directly the nuclear spin of the nearby nuclei and, consequently, an indication of the position of the electron spin in the crystal structure.

1.0 DETERMINATION OF g-FACTOR

A knowledge of the g-factor, together with the width of the absorption line, leads directly to knowledge of the atomic structure surrounding the unpaired electron. Generally, a narrow resonance line (of the order of a few gauss) when associated with a g-factor close to that for the free electron is an indication that the electron is relatively isolated from the surrounding lattice.

By determining the frequency at which the peak occurs, the g-factor can be determined to the degree of accuracy that ν and H are known. From Equation (B3) an expression for g is

$$\begin{aligned} g &= (h/\beta)\nu/H \\ &= (6.63 \times 10^{-27} / 9.27 \times 10^{-21})\nu/H \\ &= (0.71444)\nu/H \end{aligned}$$

where: ν is in MHz and H is in gauss

2.0 MEASUREMENT OF SPIN CONCENTRATION

On the assumption that an unknown EPR line has been identified (at least tentatively) with a particular defect species, any understanding of its generation or annealing kinetics depends on a further knowledge of the defect concentration (density). Measurement of the number of spins in a given mass of a specimen of known density provides such data.

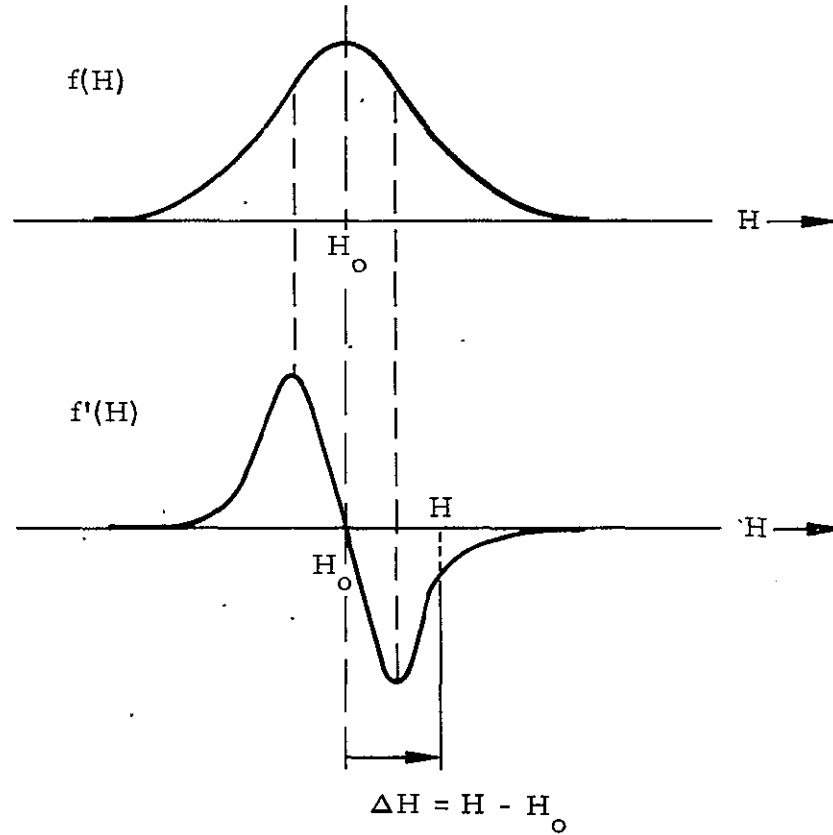
The procedure observed in this laboratory was carried out in the order indicated below:

- a. A primary standard was selected with spin concentration, line width and location similar to resonance system of interest.
- b. A primary standard was used to calibrate a secondary standard which was small enough to permit location within the cavity during EPR measurements on unknown specimens.
- c. With the calibrated secondary standard in place in the cavity, the unknown specimen is run in the cavity.

Specifically a primary standard, consisting of powered pitch diluted in powered KCl to have 3×10^{15} spins, was obtained from Varian Associates. The secondary standard was a ruby crystal. It was cemented (styrene cement) in the microwave cavity at such an orientation as to insure that its resonance line did not overlap the unknown lines displayed by the experimental specimen.

The number of spins associated with the pitch in KCl and ruby lines may be compared on the basis of the area beneath their respective absorption lines. The EPR data is usually taken in the form of the first derivative of the absorption line.

Fortunately the area A under any absorption line $f(H)$ can be simply related to an exact integral involving its first derivative $f'(H)$ as follows:



$$A = \int_{-\infty}^{\infty} f(H) dH \quad (B5)$$

Make a change of variable such that:

$$u = f(H) ; \quad \therefore du = \frac{\partial f(H)}{\partial H} dH = f'(H) dH \quad (B6)$$

$$dv = dH ; \quad \therefore v = \Delta H = H - H_0 \quad (B7)$$

Appropriate use of Equations (B6) and (B7) now permits integration of Equation (B5) by parts:

$$\int u \, dv = uv - \int v \, du$$

$$A = \int_{-\infty}^{\infty} f(H) \, dH = [f(H) \cdot \Delta H]_{-\infty}^{\infty} - \int_{-\infty}^{\infty} \Delta H \cdot f'(H) \, dH \quad (B8)$$

Noting that $f(H) = 0$ at $H = \infty$ and $H = -\infty$, Equation (B8) may be simplified:

$$A = - \int_{-\infty}^{\infty} \Delta H \cdot f'(H) \, dH = - \left[\int_{-\infty}^{H_0} \Delta H \cdot f'(H) \, dH + \int_{H_0}^{\infty} \Delta H \cdot f'(H) \, dH \right] \quad (B9)$$

Reference to the sketch of $f'(H)$ indicates that the product, $\Delta H \cdot f'(H)$ is always negative, since (either to the right or left of H_0) when ΔH is positive $f'(H)$ is negative and vice versa. Thus the integral in Equation (B9) is positive and the limits of integration are consistent with the designation of H_0 as the magnetic field intensity at the peak of the absorption line.

Graphical integration under $f'(H)$ may be carried out by means of the approximation:

$$\sum_i \Delta H \cdot f'(H) \Delta H_i = \sum_i (H_i - H_0) f'(H) \Delta H_i \quad (B10)$$

where the increment ΔH_i is taken small and is not to be confused with the "lever arm" $\Delta H (= H_i - H_0)$.

Equations (B9) and (B10) contain areas multiplied by "lever arms." This fact points up the importance of obtaining narrow lines and/or good definition of line tails. Failure to do so (as with broadened lines) increases error rapidly because of the magnifying effect of these lever arms in the integration.

The above procedure permits calculation of A(pitch) and A(ruby). The number of spins associated with the ruby crystal was then determined and used as a normalizing factor from which the number of spins associated with each of the unknown resonance lines in the experimental specimen was determined.